Ostanin, I., Anka, Z., di Primio, R. (2013): Hydrocarbon plumbing systems above the Snøhvit gas field: structural control and implications for thermogenic methane leakage in the Hammerfest Basin, SW Barents Sea. - Marine and Petroleum Geology, 43, 127-146

DOI: 10.1016/j.marpetgeo.2013.02.012

# Hydrocarbon plumbing systems above the Snøhvit gas field: structural control and implications for thermogenic methane leakage in the Hammerfest Basin, SW Barents Sea

**Ilya Ostanin*[1], Zahie Anka[1], Rolando di Primio[1], Asdrúbal Bernal[2].**

**corresponding author: ostanin@gfz-potsdam.de, Phone: +49 331 288-28614 Fax: +49 331 288- 1782*

*(1) Helmholtz Centre Potsdam - GFZ German Research Centre for Geosciences. Potsdam, Germany, Telegrafenberg, D-14473 Potsdam*

*(2) Principal Geologist - Structural Geology Analysis & Modelling, Exploration Norway, Skrugard Area, Statoil ASA, Mølnholtet 42, Harstad NO-9480 Norway*

## Abstract

Based on the analysis of the high resolution 3D seismic data from the SW Barents Sea we study the hydrocarbon plumbing system above the Snøhvit and Albatross gas field to investigate the geo-morphological manifestation and the dynamics of leakage from the reservoir. Fluid and gas escape to the seafloor is manifested in this area as mega-pockmarks 1-2 km-wide, large pockmarks (<100 m wide) and giant pockmarks 100-300 m-wide. The size of the mega pockmarks to the south of the study area may indicate more vigorous venting, whilst the northern fluid flow regime is probably characterised by a widespread fluid and gas release. Buried mega depressions and large-to-giant pockmarks are also identified on the base Quaternary and linked to deep and shallow faults as well as to seismic pipes. A high density of buried and seafloor giant pockmarks occur above a network of faults overlying an interpreted Bottom Simulating Reflector (BSR), whose depth coincides with the estimated base of the hydrate stability zone for a thermogenically-derived gas hydrate with around 90 mol% methane. Deep regional faults provide a direct route for the ascending thermogenic fluids from the reservoir, which then leaked through the shallow faults linked to seismic pipes. It is proposed that the last episodic hydrocarbon leakage from the reservoir was responsible for providing a methane source for the

formation of gas hydrates. We inferred that at least two temporally and dynamically different fluid and gas venting events took place in the study area: (1) prior to late Weichselian and recorded on the Upper Regional Unconformity (URU) and (2) following the Last Glacial Maximum between ~17-16 cal ka BP and recorded on the present-day seafloor.

## 1 Introduction

Since the onset of petroleum exploration in the Barents Sea, the Snøhvit gas discovery (1984) in the Hammerfest Basin (Fig. 1, 3) has resulted as the most successful and has been under production since 2006. With the exception of Goliat, recent Skrugard and Havis discoveries as well as a small oil find in well 7120/2-1, almost all of the proven hydrocarbon reserves were found to be gas with uneconomical residual oil (NPD, 2011). The lack of significant oil discoveries and dominance of gas have been attributed to the late Cenozoic exhumation and high latitude glaciations (Doré and Jensen, 1996; Cavanagh et al., 2006; Laberg et al., 2011). In the Barents Sea, uplift and tilting coupled with rapid erosion associated with waning and waxing of the ice sheets led to differential stress distribution, causing 1) depressurization induced reservoir gas expansion and oil-to-gas phase change (Nyland et al., 1992), 2) hydrocarbon spill out of structures due to tilting and uplift (Dore et al., 2002; Cavanagh et al., 2006), 3) Seal failure (Corcoran and Dore, 2002), 4) suppression of hydrocarbon generation due to source rock cooling (Doré and Jensen, 1996) and 5) possible, although still debated, reactivation of faults (Grollimund and Zoback, 2003; Bjørlykke et al., 2005; Brandes et al., 2010).

In sedimentary basins, recognition of active or paleo hydrocarbon seepage is extremely valuable as it provides clues regarding the present-day petroleum system, the risk associated with seal failure, *in situ* hydrocarbon volumes and their possible composition in the deeper prospective reservoirs (Heggland, 1998; O'Brien et al., 2005). Additionally, seabed fluid flow features may be associated not only with shallow gas accumulations but also slope instabilities, which may represent seafloor geohazards and impede successful seabed installations. Hydrocarbon leakage from the Snøhvit, Albatross and Askeladd fields (Fig.3) has been previously reported as large gas anomalies causing acoustic wipe-out zones

(Ostanin et al., 2012), whilst a paleo oil-water contact suggested that reservoirs were once filled with significantly larger volumes of hydrocarbons than today (Linjordet and Grung-Olsen, 1992). Leakage has been postulated to have taken place along the major tectonic faults, bounding the reservoir structures (Linjordet and Grung-Olsen, 1992; Ostanin et al., 2012), whilst seabed pockmarks and acoustic flares manifest possible recent fluid leakage into the hydrosphere (Judd and Hovland, 2007; Chand et al., 2012). Nonetheless, a detailed analysis of all the elements of the hydrocarbon plumbing system dynamics has not been carried out before.

In general, evidence of fluid flow is manifested on the seabed as metre- to- kilometre scale pockmarks, seep mounds, acoustic flares (Judd and Hovland, 2007), mounded structures (Anka et al., 2012) as well as gas chimneys and seismic pipes (Cartwright et al., 2007; Løseth et al., 2009). The fluid and gas seeps also attract diverse benthic and chemosynthetic communities, making them an integrated part of the deep sea ecosystems (Judd and Hovland, 2007). In the subsurface, ascending gas and fluids may also be temporarily or permanently trapped en route to the surface, leaving imprints of their former flow within the stratigraphic successions. They can be inferred from geophysical datasets in form of amplitude anomalies caused by the acoustic impedance contrasts associated with the velocity and density changes compared to the surrounding rock (Brown, 2004; Løseth et al., 2009). Shallow gas accumulations can cause scatter and attenuate seismic waves while disrupting seismic records causing chaotic, acoustic turbidity, wipe-out zones, and artificial sagging of the reflections due to gas presence in the overlying strata (Løseth et al., 2009). Gas saturations as low as 10% in the sediment porespace can potentially cause a significant drop in P wave velocity and may be detected by seismic methods, depending on the impedance contrast and the data resolution (Brown, 2004; Andreassen et al., 2007).

Disturbances having a stacked or columnar nature are termed "seismic pipes" and are considered to be vertical fluid and gas migration pathways affecting at times over 1 km of sediments (Cartwright et al., 2007; Huuse et al., 2010; Moss and Cartwright; Løseth et al., 2010). Seismic pipes are usually circular to sub-circular in plan-view and have vertical to sub vertical geometries, characterised by vertical zones of deteriorated seismic signal. They have been postulated to be caused by hydraulic fracturing of the sealing stratigraphy by rapidly ascending gas and fluids escaping from overpressured hydrocarbon accumulations (Cathles et al., 2010). Inside the seismic pipes intense fracturing dominates, thus increasing permeability and reducing seal integrity, allowing fluids to flow (Cartwright et al., 2007; Huuse et al., 2010). However, some seismic pipes may be plugged by hydrate cementation, releasing methane at slow rates (Plaza-Faverola et al., 2010). Seismic pipes may also terminate in blow-out events on the seabed, forming pockmarks, depending on their intensity and overpressure regime (Cartwright et al., 2007). They are discriminated from seismic processing artifacts as they exhibit both structural and stratigraphic control upon their development, such as their location above structural traps or faults (Cartwright et al., 2007; Huuse et al., 2010). Seismic pipes are differentiated from gas chimneys, which are wide zones of deteriorated seismic signal (wipe-out, chaotic reflections, velocity pull-downs), associated with low velocity zones caused by shallow gas accumulations or vertical gas migration (Løseth et al., 2009). Stacked pockmarks can be also related to tectonically induced changes in the stress field (Baraza and Ercilla, 1996) and may imply multiple phases of fluid flow. Although most seafloor pockmarks appear dormant, their activity may be episodic driven by climatic undulations, tectonism/earthquakes (Judd and Hovland, 2007), sea level (Andresen and Huuse, 2011) tide/storm waves (Holbrook et al., 2002), or waning and waxing glaciations (Plaza-Faverola et al., 2011).

This study aims to unveil the fluid leakage dynamics and history above the Snøhvit gas field in the Hammerfest Basin, in order to determine what effects the tectonic uplift and multiple phases of glacial cycles in the SW Barents Sea had on the hydrocarbon reservoirs. We analysed a commercial 3D seismic dataset focusing on the identification of manifestations of fluid flow and their interaction with structural and stratigraphic elements of the basin. Our aim was to characterise the pathways, controls and timing of hydrocarbon leakage, termed collectively here as the hydrocarbon plumbing system.

## 2 Geological evolution of the study area

The study area is located in the Hammerfest basin (Fig. 1), which is one of the several basins separated by structural highs comprised within the epicontinental Barents Sea (Faleide et al., 2008). The opening of the Norwegian-Greenland Sea to the west has had a significant influence on the Cenozoic development of the structural and sedimentation regimes in this area (Faleide et al., 2008). The fault architecture in the Hammerfest Basin during Middle Jurassic consists of EW trending normal faults formed as a result of Kimmeridgian tectonics (Figs. 1, 2, 3). These faults were reactivated during the Hauterivian-Barremian (Lower Cretaceous), while the NS trending fault activity took place during Aptian (Lower Cretaceous) and Cenomanian-Campanian (Upper Cretaceous) times (Ostanin et al., 2012). Cenozoic episodic uplift resulted in three exhumation episodes dated to the Paleocene (60-55 Ma), late Eocene (36-35 Ma) and Late Miocene (7-5 Ma), coincident with Atlantic tectonic episodes (Green and Duddy, 2010). Fault reactivation in the Hammerfest Basin over the Albatross and Askeladd structures (Fig. 3) was dated to late Paleocene- early Eocene, associated with NS and EW fault trend reactivation (Ostanin et al., 2012). In the Hammerfest Basin (HB), prograding clinoforms reflect changes in tectonic and sedimentation regimes as local highs were uplifted (Faleide et al., 2008). Complete lack of Neogene strata in the HB is a consequence of Miocene uplift and erosion of 800-1000 m of sediments (Cavanagh et al., 2006; Green and Duddy, 2010).

The Pliocene-Pleistocene periods were influenced by ice sheets that prevailed in the Northern Hemisphere from around 2.7 Ma (Knies et al., 2009). The Barents Sea Ice Sheet (BSIS) prominent during the Weichselian glaciation covered an area over $5*10^6$ $km^2$, centered on present-day Norway and Sweden, reaching ice thicknesses around 1.5 km over the study area (Svendsen et al., 2004). The full extent of the BSIS during the Last Glacial Maximum (LGM) is shown in figure 1. Numerous Megascale Glacial Lineations (MSGLs: elongated linear grooves and ridges parallel to trough long axis (Clark, 1993)) have been mapped along the seabed and the glacial surfaces in the Barents Sea and indicate that the deglaciation was accompanied by fast flowing ice streams and sub-glacial sediment deformation at the base of the sheet, which controlled the drainage patterns of the BSIS (Ottesen et al., 2005; Andreassen et al., 2008; Winsborrow et al., 2010). During the last 2.7 Ma, Pliocene-Pleistocene glacial advances and re-advances resulted in erosion of over 1 km of sediments, half of that amount may have taken place from 0.7 Ma due to erosion beneath fast moving ice streams (Laberg et al., 2011), terminating in large sediment depocentres along the western margin (Fig. 1), eg. the Bear Island Trough mouth fan (Andreassen et al., 2008; Faleide et al., 2008; Laberg et al., 2010). The Hammerfest Basin was covered by an ice sheet at ~19 cal ka BP (Winsborrow et al., 2010) and became ice free by ~17-16 cal ka BP with operating ice streams (Rüther et al., 2011), whilst complete deglaciation of the Barents Sea is proposed around 15 cal ka BP (Svendsen et al., 2004; Ottesen et al., 2005; Winsborrow et al., 2010; Rüther et al., 2011). As the ice retreated onshore, ice loss due to calving was no longer possible, slowing down the deglaciation. In the Barents Sea, deglaciation was likely to have been coeval with rising sea level (Clark et al., 2009), whilst ice was quickly removed through calving (Vorren and Laberg, 1996). The present-day morphology of the Barents Sea is characterised by relatively shallow water depths of less than 500 m, with the deepest parts of the shelf defined by several troughs (Fig. 1) created by paleo ice streams that operated during the deglaciation (Ottesen et al., 2005; Laberg et al., 2010). Low sedimentation rates followed the last glacial maximum, with deposition of thin layers of glacial till and Holocene clays (Chand et al., 2012).

The main sequences and boundaries discussed in this work correspond to the present-day Seabed (Top Nordland), the Upper Regional Unconformity (URU), Campanian (Kviting Fm/Kveite Fm) and the Bajocian (Stø Fm, Fig. 2). The URU is an angular unconformity separating dipping, preglacial Cenozoic bedrock from the overlying glacigenic sediments (Solheim and Kristoffersen, 1984). It represents the oldest glaciogenic surface, developed by erosions during several glaciations on the continental shelf (Andreassen et al., 2008) and marking the switch from glacial erosion to an aggradational regime (Faleide et al., 2008) . The age of the URU is thought to postdate 2.6 My, although a younger age of 0.7 My has also recently been suggested (Laberg et al., 2011). In any case, its age varies across the Barents Sea shelf and is controlled by the latest period of erosion. The Cenozoic (Paleocene-lower Eocene) succession consisting of westerly dipping strata is cross cut by regional reactivated EW and NS faults, as well as intra Paleocene- E. Eocene faults (PEEFs) linked to the Campanian interval, related to reactivation of polygonal fault networks (Ostanin et al., 2012). This interval contains the gas escape anomalies, which will be described later on. The Cenomanian-Campanian interval is characterised by a thin tier of polygonal faults (Fig. 2), crosscut by regional EW and NS trending faults, which were reactivated during early Paleocene - Early Eocene (Ostanin et al., 2012). The main hydrocarbon reservoir of the Snøhvit, Albatross and Askeladd fields is located in the Jurassic Stø Fm (Fig. 2, 3).

## 3 Methodological approach

### 3.1 Database

The study was carried out using a industry-quality 3D seismic reflection volume (STO306) located over the Snøhvit and Albatross gas fields, complimented by an older 3D seismic cube situated over the Askeladd gas field (Fig. 3). Additionally, regional 2D seismic profiles were also interpreted to extend the mapping of fluid flow features regionally. The STO306 survey covers an area of 970 $km^2$, with the inlines and cross lines oriented NS and EW respectively. The data have been processed to zero-phase, normal European polarity (SEG reverse), with the positive amplitude (black) corresponding to a decrease in acoustic impedance (soft reflection) and the negative amplitude (red) marking an increase (hard reflection) in acoustic impedance (Brown, 2004). A sampling interval of 4 ms and bin size of 12.5 m by 12.5 m, as well as 3D migration, ensure a detailed geomorphological interpretation with minimal spatial aliasing, thus the horizontal resolution is comparable to the vertical resolution. The survey is dominated by frequencies between 30-50 Hz, resulting in a vertical resolution ($\lambda/4$) of ~12.5 m, (using an average sediment velocity of 2 $kms^{-1}$). The ST8320 3D seismic volume covers an area of 420 $km^2$, consists of zero phase normal European polarity data, sampled at 4ms and binned at 25 m by 25 m. The dominant frequency range of the survey is 20-40 Hz, with a vertical resolution of ~16.5 m (using 2 $kms^{-1}$ as average sediment velocity). The 2D seismic data in the Cenozoic section are dominated by frequencies ranging between 10-30 Hz, resulting in vertical resolution of ~20m (using 2 $kms^{-1}$ as average sediment velocity).

### 3.2 Seismic interpretation methods

We focused our analysis on the geospatial distribution of leakage indicators between two prominent horizons, the URU and the contemporaneous seabed (Fig. 2). We used commercial Schlumberger Petrel Exploration and Production software package, versions 2009-2011.1 for loading and interpretation of the 3D seismic volumes. Interpretation of seismic horizons was carried out using the zero-crossing points between peaks and troughs as this method enables very detailed geomorphologic features to be picked out without risk of clipping or smoothing artefacts in the final maps (Bulat, 2005). We have also applied a series of seismic attributes such as root-mean-squared (RMS) amplitude, variance, dominant and instantaneous frequency. The seismic variance volume attribute was used to delineate boundaries and faults and has been used in different settings to aid structural interpretation (e.g. Ostanin et al., 2012).Variance attribute is a refined algorithm of the Coherency cube (Bahorich and Farmer, 1995) and is aimed at a more detailed edge-isolation method (Van Bemmel and Pepper, 2000). Trace-to-trace variability is computed in 3D over a sample interval, where seismic discontinuities and boundaries produce high-variance values due to significant differences in neighbouring waveform. The dominant frequency attribute picks out subtle changes at a high resolution, while the RMS amplitude highlights sudden acoustic impedance contrasts. Both were used to infer lithology changes and potential effects of fluid saturations within the seismic volumes. Although available well logs do not pass through any of the features identified in this study, they were used to estimate the ages of the stratigraphic horizons, constrain the lithologies derived from well cuttings description, and extrapolate depths using available checkshots in the Paleocene-Eocene strata, where the gas anomalies occur.

Mapping of the seabed was carried out using semi-automated interpretation and further generation of two-way-time (TWT) maps, volume based as well as horizon based attributes. Attribute volume rendering was used to identify possible structures beneath seafloor depressions (pockmarks), such as faults, acoustic pipes and amplitude anomalies. Pockmark average width was measured along variance time-slices, variance along selected horizons and crest to crest using inlines and cross-lines. They were then grouped according to size classes. Due to limitations in seismic resolution at the seabed, depressions smaller than 30 m (using 3D migration Fresnel zone radius relationship of ~λ/2 (Brown, 2004), water velocity of 1500 $ms^{-1}$ and an average frequency along the seabed of 25 Hz) were not imaged. High resolution multi-beam bathymetry would be required to analyse smaller pockmarks. Depth conversion from two way travel time (TWT) was carried out using constant velocities of 1750 $ms^{-1}$ for the Quaternary sediments above the URU and 1500 $ms^{-1}$ for the water column (Saettem, 1991). Pockmark mapping on the older ST8320 survey was not carried out due to low bin spacing of 25 m and thus lower horizontal resolution of the data compared to the STO306 survey.

### 3.3 Hydrate Stability Calculations

We performed Pressure-Volume-Temperature (PVT) calculations, using commercially available software (PVTSim V.17, Calsep, Dk), to estimate the equivalent gas composition at the depth of the gas anomaly 1 BSR anomaly. In order to do this, we used reported in-reservoir natural fluid compositions and calculated the changing physical properties and composition as function of stepwise pressure and temperature reductions (PT flashes). Additionally, the CSMHYD programme (Sloan, 1990) was used to predict the thermodynamics of stable hydrate structures (I and II) for a given composition, temperature and pressure conditions with and without salt as inhibitor.

## 4 Results

### 4.1 Evidence of glacial erosion processes

The seabed is characterised by a large number of curvilinear furrows of varying relief (4-11 m), lengths (1-16 km) and widths (40-200 m), whilst trending 50-105N and having a linear, curved," v" and "u" shape (Fig. 4a). Seabed furrows are particularly well preserved and abundant in water depths shallower than ~330 m. We interpret these features as iceberg ploughmarks formed due to the scouring of the seabed sediments by wind and current-transported icebergs, resulting from glacier calving in deep waters during the late Weichselian (19 - 15 cal ka BP) deglaciation phase (Judd and Hovland, 2007; Winsborrow et al., 2010). Similar ploughmarks have been reported in many other areas of the Barents Sea (Rafaelsen et al., 2002; Andreassen et al., 2008). Acquisition footprint is parallel to the inline direction trending 0°N and is discriminated from the real geomorphological features. In water depths ranging from ~337-360 m (450-480 ms TWT) also parallel and sub-parallel lineations exist, 0.2-5 km in length, trending 135-145N (Fig. 4a), interpreted as MSGLs (Andreassen et al., 2008). The lineations are crosscut by EW trending ploughmarks, implying that ice streaming was pre-ceded by calving of the marine ice sheet. In contrast to the seabed, we observe that a much larger area of the URU surface is affected by 140-160N trending MSGLs (Fig. 4b). Whilst separated by ~40 m (~50 ms TWT), this indicates that both the seabed and the URU underwent significant erosion while the marine ice sheet was retreating and vast volumes of sediments were likely to have been eroded at those times. The ploughmarks on the URU are linear depressions, trending 2-12N, having a length between 0.2-1.2 km and seem to crosscut the MSGL (Fig. 4b).

## 4.2 Pockmarks and buried pockmarks

*On The Seabed*

Overall, 297 pockmarks were identified on the seabed and classed into large pockmarks (up to 100 m wide, Table 1, Fig. 5), giant pockmarks, (from 100-300 m wide) and mega-pockmarks (exceeding 1 km in width, Fig. 6). The latter are exclusive to the SW corner of the study (Fig. 3, 7). Overall, 46 pockmarks fall into the 50-100 m diameter range, 60 pockmarks are between 100 and 200 m and 9 pockmarks are 200-300 m wide, with the 100-300 m pockmarks termed "giant" (Table 1, Fig. 5g). Higher density of large and giant pockmarks is found in the deeper parts of the seabed ~315-350 m (470-420 ms TWT), particularly in the area affected by the MSGLs, whereas the two mega-pockmarks are located in the area affected by iceberg ploughmarks with water depths ranging from ~276-284 m (369-379 ms TWT) (Fig.

6a, 7a). Additionally, there seems to be an inverse correlation between the thickness of the Quaternary cover and the frequency of seabed pockmarks (Fig. 7b). Thinner patches of Quaternary strata (40-60 ms TWT) have higher pockmark frequency. The NW cluster of seabed pockmarks is located over an identified shallow gas anomaly (Fig. 3), suggesting a possible fluid/gas source responsible for the pockmarks in that area. The central part of the study appears to be unaffected by pockmarks wider than 30 m, which might suggest harder sediments as pockmarks generally develop within soft, fine grained cohesive sediments (Judd and Hovland, 2007).

*On The Upper Regional Unconformity (URU)*

Overall, 324 pockmarks have been identified and mapped on the URU (Fig. 7c). They are mainly circular in map view, occurring in clusters or individually, with depths ranging from 7-20 m (8-23 ms TWT) and from 40-400 m in width (Fig. 5e, f). Smaller circular depressions have also been observed, but only features larger than the vertical and horizontal resolution limits are included in the maps. Large concentrations of pockmarks on the URU occur in two dense populations: to the north-western and northern parts of the study (Fig. 7c). The higher density of pockmarks on the URU also coincides with the largest concentrations of seabed pockmarks, however the URU surface preserves a much larger number of pockmarks. Seismic profiles across the buried fossil pockmarks reveal that they are covered by relatively undisturbed internal reflections, indicating inactivity following the deposition of Quaternary sediments (Fig. 5e,f). Above the gas anomalies 1 and 2 (Fig. 3), an area of 80 $km^2$ on the URU and a smaller area of ~60 $km^2$ on the present-day seabed is affected by pockmarks (Fig. 7).

### 4.3 Mega pockmarks and depressions

*On The Seabed*

Two circular depressions, interpreted as mega-pockmarks have been identified in the SW corner of the study area, located along the hanging wall of the NS fault trace(Figs. 3, 6c, e 7a, ). They have smoothly dipping edges and are crosscut by numerous ploughmarks, indicating that these features predate the last episode of iceberg scouring. The northernmost mega-pockmark 1 is 1.9 km wide and around 50 m deep (68-74 ms TWT) with sides dipping ~3°. It is crosscut at its centre by a 65°N trending plougmark and the underlying seismic reflections are discontinuous, affected by velocity pull downs and acoustic blanking (Fig. 6c, d). Mega-pockmark 2 is slightly smaller, 1.7 km wide and around 45 m deep (57-65 ms TWT), with sides dipping at ~2°. Its edges are crosscut by several ploughmarks trending 74N and 112N. Similar to mega-pockmark 1, it is underlain by noisy seismic reflections and zones of acoustic blanking (Fig. 6e).

*On The Upper Regional Unconformity*

A composite surface of the URU reveals six kilometer scale, circular-to-elongated (trending 140-150N) depressions, two of which (1' and 2') are situated underlying the two seabed mega-pockmarks (1 and 2) described above (Fig. 6b, c, d, e, f).

Depression 1' is circular in map view, 1.9 km wide and between 20-39 m deep (23-45 ms TWT), with smooth walls dipping between 1-2°, interpreted as a mega pockmark. From the TWT map inside depression 1 we distinguish several smaller circular large to giant pockmarks, 90-170 m across as well as a crescent shaped depression (Fig. 6b). The latter is around 600 m long , 90 m wide and less than 10 m deep, and may have resulted from the coalescence of several giant pockmarks. There is a striking similarity between this feature and the pockmark families reported by Hovland et al. (2010) near the Troll Field (mid Norway), which consist of major pockmarks containing satellite pockmarks caused by a continuous flow and development of a carbonate plug following a main escape event.

Depression 2' comprises a circular depression linked to an elongated depression (Fig, 6b, e) with smooth walls dipping <1°, and the western wall having a steeper slope gradient. This feature is similar to a composite pockmark and may have formed by coalescence of two separate mega pockmarks. The depression is 12 - 21 m deep (14-24 ms TWT), 1.2-1.6 km wide, having a length of 3.8 km with the long axis trending 150N.

Depression no. 3' is 0.5 km to the SW of from depression no. 2' (Fig. 6b). This depression is rather elongated, 3 km long and 1 km wide, with the long axis trending 165N. It is around 29-38 m deep (34-44 ms TWT) and presents smooth wall dips of around 1.7°. The depression fill is characterized by amplitude brightening and a dim spot (Fig. 6f), which could imply gas saturation or change in lithology Since only a few per cent of free gas in the sediment pore space can significantly reduce the P-wave sediment velocity, often resulting in an enhanced reversed polarity seismic reflection (Andreassen et al., 2007), the anomaly may not necessarily imply a geohazard. However there could potentially be a risk for geotechnical installations (Judd and Hovland, 2007).

Depression no. 4' trends 160N, is 2.9 km long and 1.3 km wide and is broken up into two 12-14 m deep (14-20 ms TWT) depressions. The southeastern extent of this feature is tapered by the edge of the 3D seismic survey (Fig. 6b).

Depression no. 5' is located over 2 km west of depression 4' (Fig. 6b). It appears roughly circular, with steep sub-vertical walls, and another smaller circular depression 0.3 km to the south of the main depression. It is E-W elongated, 1.7 km long and 1.6 km wide. The depth of this depression ranges between 17-24 m (20-26 ms TWT).

Another interesting feature identified 0.5 km to the north-west of depression 5' is a linear depression no 6', 3.3 km long and 0.5 km wide, whose long axis trends 88N (Fig. 6b). The sides are steeper than the other described depressions 2'-5', dipping 5-6°, whilst its depth ranges from 24-31 m (28-36 ms TWT). A possible merging of smaller aligned pockmarks could be the cause for this linear depression. Since a Paleocene-Eocene 86N striking fault underlies this feature (Fig. 6i), a structural control on the linearity cannot be ruled out. Similar features have been observed elsewhere in the Barents Sea and West Africa and attributed to deeper thermogenic fluids migrating along fault planes (Pilcher and Argent, 2007; Chand et al., 2012).

*Structural elements beneath the URU depressions*

Figure 8b summarizes the structural elements underlying the mega-pockmarks identified on the URU surface. The Paleocene-Eocene, Cretaceous and Jurassic successions are cross cut by the EW and NS trending reactivated faults and their conjugate pairs, some of which are bounding the main present day hydrocarbon reservoirs of Snøhvit, Albatross and Askeladd (Figs. 2, 3, 8b). The Upper Cretaceous (Cenomanian-Campanian) interval (Fig. 3) is characterised by polygonal fault networks and is crosscut by the reactivated faults (Ostanin et al., 2012). Sediments of Paleocene-Early Eocene age overlying the Upper Cretaceous unconformity are affected by numerous normal faults, linked to the polygonal faults interval beneath and the reactivated tectonic faults, forming a dense network of interconnected faults (Ostanin et al., 2012). The Paleocene - E. Eocene sediments also host the enhanced reflections, interpreted as gas anomalies (Fig. 2, 3).

## 4.4 Gas anomalies and BSRs

*Gas "anomaly 1 (A1)"*

This is the larger of two identified amplitude anomalies, having an extent of ~50 km$^2$ and causing severe acoustic blanking and velocity pull-downs beneath it (Fig. 3, 9a, b). The top of the anomaly is located between 680-760 m (680-760 ms TWT), based on nearby wells and checkshots, which also agrees with a depth conversion using 2000 ms$^{-1}$ as average sediment velocity. The top of gas anomaly 1 is characterised by a soft reflection (positive amplitude loop, blue) marking a decrease in acoustic impedance, which has a reversed polarity, compared to the seabed (red) reflection (Fig. 9a, b). Below gas anomaly 1 seismic amplitudes are dimmed, leading to wipe-out effects, whilst deeper reflectors are pulled down (Rønholt et al., 2008; Ostanin et al., 2012). Additionally, the high-amplitude reversed-polarity reflections appear to be crosscutting the reflections from the westerly dipping Paleocene strata. All these characteristics led us to interpret this reflection as a bottom simulating reflector (BSR). The BSR represents indirect evidence of gas hydrate in the overlying sediments, where the base of the gas hydrate stability zone (GHSZ) is controlled by temperature and pressure conditions, gas composition, presence of water and type of hosting sediment the hydrates (Sloan, 1990). Seismic velocity down to the BSR usually increases, with a sudden drop below the BSR due to presence of free gas (Singh and Minshull, 1993).

The EW reactivated faults bounding the deep Jurassic hydrocarbon reservoir and the NS trending fault (curving westward) crosscut the gas anomaly 1 (Fig. 3). The reactivated faults are sealed below the URU (Figs. 5d, 6c-e; (Ostanin et al., 2012)) and are directly linked to structures containing proven hydrocarbons (Figs. 2, 8b), which suggests possible upward migration paths for thermogenic fluids (Ostanin et al., 2012). Within the Paleocene-Eocene, a network of faults crosscuts the gas anomaly 1 forming a dense network of interconnected faults. The intra Paleocene-Eocene faults that pass through the gas anomaly 1 create fault-bounded amplitude anomalies, which suggests their control on gas/fluid migration (Fig. 9 a, b). These faults lead to vertical 50-100 m wide acoustic discontinuities interpreted as seismic pipes (Figs. 5e, 9). Seismic pipes are characterised by low amplitudes and high dominant frequencies (30-45 Hz) within the pipe structures compared to surrounding seismic reflections. Several seismic pipes contain low frequency (10-20 Hz) shadows within the pipe structure. The seismic pipes are imaged by the variance attribute as circular discontinuities and some of them terminate in buried pockmarks on the URU (Figs. 5e, 9 b), whilst others penetrate the Quaternary strata terminating in seabed pockmarks (Fig. 9c).

*Gas "anomaly 2 (A2)"*

This anomaly is located at ~630-680 ms TWT (630-670 m), characterised by a broad zone ~18 km$^2$ of enhanced reflections, which show strong polarity reversals in EW profiles underlying acoustic blanking and some possible associated flat spots (Fig. 10 a). The seismic character underlying the anomaly is composed of semi-chaotic reflections caused by partial P-wave attenuation and velocity pull-down effects, yet the effects of acoustic masking are not as dramatic as in the gas anomaly 1. The southern boundary is related to an EW trending reactivated fault (Fig. 3) , which also crosscuts the gas anomaly 1 (Ostanin et al., 2012). Some of the intra Paleocene- E. Eocene faults link the EW faults to the gas anomaly 2. However, unlike gas anomaly 1, gas anomaly 2 is not bounded or crosscut by the interconnected intra Paleocene-Eocene faults (Fig. 10 a). Above gas anomaly 2 there are numerous, vertical zones of low impedance/vertical acoustic wipe-out (20-80 m wide), with higher dominant frequencies (30-40 Hz), within them.

*Gas hydrate stability calculations*

The results of the Pressure-Volume-Temperature (PVT) calculations predict that the gas leaked from Snøhvit , which has original methane contents of 86-87 mol% under reservoir conditions, would contain between 89 and 90 mol% methane at the level of the observed gas anomaly 1 (750 m depth and 15° C).

We therefore estimate the phase-stability curves for hydrate structures I and II (Sloan, 1990) considering three methane contents: 100, 96 and 90 mol%. , The last two cases include respectively 4 and 10 mol% higher-order hydrocarbon gases, namely ethane and propane (Fig. 11). The presence of salt in the pore water inhibits the formation of hydrates, hence, higher pressures are needed to form hydrates (Sloan, 1990). Thus, if all factors remain the same, the effect of increasing pore water salinity reduces the GHSZ thickness by ~100 m. We take this into account using a sea water approximation of 3.5 mole% NaCl. Three scenarios have been constructed for the hydrate stability fields: for the glacial periods (Fig. 11 a), interglacial following the LGM (Fig. 11 b), and at present-day conditions (Fig. 11 c) with and without pore water salinity as a hydrate inhibitor (Fig. 11 a, b, c). The controlling factors on the stability of hydrates in the study area are: 1) pressure (water depth/effect of glaciations), 2) bottom water temperature, 3) geothermal gradient, 4) gas composition and 5) pore water salinity. Additionally, the sea bottom temperature is another influential parameter that coupled with pressure variations can result in dramatic shifts in the GHSZ. The present-day water depth in the Hammerfest basin ranges between 240-360 m in the study area, where the deeper parts are characterised by the MSGLs (Fig. 4a). We use a water depth of 320 m (closest to gas anomaly 1 and 2), average geothermal gradients of 30° and 35° Ckm$^{-1}$ (NPD, 2011) and a seabed temperature of 6ºC (NODC, 2011; Nickel et al., 2012). However higher geothermal gradients may exist near faults, causing locally decreased thickness of the GHSZ. The results show that although the gas hydrates are unstable for a pure methane system, the presence of higher order hydrocarbons (eg. 90 mol % Methane) increases the thickness of the GHSZ.

For the time immediately following the LGM (~17 cal ka BP) we estimate the paleo-water depth to be 110 m lower than the present (Fleming et al., 1998). We therefore assume a water depth of 200 m to estimate the possible effect ice unloading had on the GHSZ, keeping the geothermal gradients constant (30° and 35 °Ckm$^{-1}$) and using a seabed temperature of 3° C during interglacials, assuming it was 2-3 °C colder than today (Archer et al., 2004). The results show that following the ice retreat, the GHSZ formed by a thermogenic gas hydrate system (95-90 mol% methane) may have been slightly shallower than today.

During the LGM, we assume ice thickness of 1700 m over the SW Barents Sea (Svendsen et al., 2004). Assuming 200 m water depth at the time immediately preceding glaciation, the depression created beneath an ice sheet due to glacial loading, will be approximately 0.27 the total ice thickness (Benn and Evans, 2010). This would imply that 659 m of ice would have been below the water level, with 1041 m of ice above it (Fig. 11 a). Numerous ice streams on the Barents Sea seabed indicate the temperature at the base of the ice sheet during the deglaciation must have been close to pressure melting, around 0 ºC (Winsborrow et al., 2010) which is in agreement with recorded present day Antarctic ice stream basal temperatures (Engelhardt and Kamb, 1993). Assuming a constant geothermal gradient of 35 °Ckm$^{-1}$, we estimate that a thick GHSZ existed beneath the BSIS during the LGM, exceeding 300 m below the ice base for a 100 mol% methane hydrate system, or even 600 m for wet gas compositions (90 mol% methane).

# 5 Discussion

## 5.1 Structure II gas hydrates and existence of hydrocarbon plumbing systems

Since the production of thermogenic methane due to cracking of organic matter to methane would be produced at temperatures starting from 80-90° C (Kvenvolden, 1995), gas hydrate formation from thermogenic methane must result from an upward flux of methane into the GHSZ. Migration pathways such as deep reactivated faults could provide direct routes from deeper hydrocarbon reservoirs or kitchen areas into the GHSZ (Hyndman and Davis, 1992; Gay et al., 2006; Ostanin et al., 2012).

Unlike biogenic methane related to bacterial activity, the thermogenic methane seepage is sourced at greater depths either from maturation of source rocks or from leaking hydrocarbon reservoirs. In the formation of gas hydrate, thermogenic methane content may range from 27-97 mol% while biogenic methane generally contains over 99% methane (Kvenvolden, 1995). Since the total organic carbon (TOC) content of the late Weichselian glaciomarine sediments is lower than 2% (Boitsov et al., 2011) and this amount would be too low to produce biogenic methane that could explain the observed seabed pockmarks (Solheim and Elverhøi, 1985), a deeper thermogenic source of gas must be present. Geochemical studies conducted at active and paleo seepage sites near Spitsbergen in the Barents Sea found higher order hydrocarbons in bottom waters and shallow sediments, indicating that deeper thermogenically derived fluids have migrated to the surface through reactivated faults (Knies et al., 2004). Additionally, gas flares have been observed along the Ringvassøy Loppa Fault complex (Fig. 1) suggesting a deep source of fluids and that fluid migration occurs along deep tectonic faults (Chand et al., 2012). Moreover, the lack of present-day microbial activity in the pockmarks on the Loppa high (Fig. 1) points to their inactive or "fossil" nature and that they were likely to have formed after glacial retreat following the LGM (Chand et al., 2012; Nickel et al., 2012).

The depth of the BSR in this study could be related to the gas composition, as increasing the thermogenic gas composition, (Ethane, Pentane and Propane, Fig. 11) increases the depth of the GHSZ

Alternatively the depth of the BSR (Fig. 9a) could indicate heat flow variability, however further work would be required to test this hypothesis. Previous studies in the Barents Sea, west of the Loppa High and around the Bjørnøyrenna Fault Complex have reported similar occurrences of BSR anomalies, related to gas hydrates (Andreassen et al., 1990; Løvø et al., 1990; Laberg and Andreassen, 1996; Laberg et al., 1998). The BSR anomalies occur near major deep routed faults (Laberg et al., 1998), which suggests a deep possibly thermogenic source of fluids. Thus, we propose a similar process for the thermogenic gas leakage from the reservoirs and formation of the observed BSR anomaly in the study area.

## 5.2 On the origin of the mega-pockmarks and depressions

### *5.2.1. Pockmarks associated to gas anomalies*

The plumbing system above gas anomaly 1, interpreted as a potential BSR (Fig. 9), is composed of shallow and regional reactivated faults (Ostanin et al., 2012) that penetrate the gas anomaly and lead to seismic pipes, which terminate in buried and seabed pockmarks (Figs. 5e, 9). To test whether the gas anomaly 1 represents indeed a BSR indicating base of the GHSZ ,we computed the thermodynamic stability curves using CSMHYD program (Sloan, 1990) for gas hydrates with different compositions (Fig. 11) . The top of gas anomaly 1, which lies at a depth of~740 m (740 ms TWT, using average sediment velocity of 2 $kms^{-1}$), can be correlated (±~50 m) to the estimated e base of the GHSZ for gas hydrates containing 90% methane, 7% ethane and 3% propane, which is the estimated gas composition from the Snøhvit gas field at the depth of the gas anomaly 1 (see PVT calculations in methodology, section 3.3). Hence, the gas anomaly 1 probably represents the base of hydrate stability zone and indicates the possible existence of hydrate-rich sediments overlying the anomaly, with free gas present beneath the hydrate deposits. In turn, this also supports our initial interpretation of the gas anomaly 1 as a BSR.

The locations of the faults in relation to the seismic pipes suggests that they have served as conduits for fluids originating from the underlying free gas zone. Fluids probably migrated upwards via those faults to about 500 m (~500 ms TWT, using an average sediment velocity of 2 $kms^{-1}$), where acoustic pipes formed at the fault tip terminations as a result of capillary seal failure (Clayton and Hay, 1994; Cathles et al., 2010). If overpressure develops beneath the hydrate layers, exceeding the so called the "critical gas column thickness", fault slip will take place in the overlying sediments (Flemings et al., 2003), allowing overpressure to be periodically relieved as the free gas beneath the GHSZ is bled off (Hornbach et al., 2004), whilst hydrofracture may result in creation of new fault networks. Since leakage along a fault plane may happen periodically or in bursts (Haney et al., 2005), some faults may have been leaking and conducting fluids more than once. Thus, repeated overpressure buildups could have triggered the fluid escape events observed on the two separate chronological surfaces: the URU and the present-day seabed. The plumbing system above gas anomaly 2 comprises acoustic pipes sourced from the top of the enhanced reflections from gas anomaly 2, terminating in pockmarks on the URU and the seabed. Shallow faults do not seem to play a role in controlling the fluid transport to the surface (Fig. 10). Acoustic pipes indicate seal-bypass systems and result in highly focused vertical fluid flux (Berndt, 2005; Cartwright et al., 2007). When the subsurface pressure due to ascending fluids is sufficiently high, the seal is overcome due to hydrofracture , resulting in generation of a fracture network, which then leads to formation of an acoustic pipe structure (Clayton and Hay, 1994; Huuse et al., 2010). Some of the seismic pipes can be traced up to the URU, whilst some are also affecting the Quaternary and leading to seabed pockmarks (Fig. 10 b). This implies that gas anomalies 1 and 2 are active today and likely to have formed as a result of long-lasting fluid leakage from the URU to Present day. Additionally, the higher frequency response present within seismic pipes may be related to carbonate or hydrate cementation present within the pipes (eg. Plaza-Faverola et al., 2010), whereas the frequency shadows may indicate absorption of high frequencies due to the presence of fluids or gas accumulations within the pipes. Whilst burial of the URU pockmarks indicates cessation of fluid and gas escape through the pipes, the fact that some pipes also lead to seabed pockmarks shows evidence of a more recent leakage event. Interestingly, the top of anomaly 2 (~720 m (720 ms TWT, using 2 $kms^{-1}$ as average sediment velocity)) is close to the base of the GHSZ using the hydrate stability phase diagram for a 90 mol% methane, 7% ethane and 3% propane composition (Fig. 11 c). This implies that the possible gas hydrate layer above the gas anomaly 2 has been breached by vertical fluid conduits, providing a direct route from the free gas zone below the GHSZ to the seafloor. Similar scenarios have been reported in other settings eg. Mid Norwegian margin, Blake Ridge, the Congo Basin and the Malvinas Basin, where acoustic pipes originate within the free gas layers, penetrating the BSR and leading to seabed pockmarks (e.g. Gorman et al., 2002; Bünz et al., 2003; Gay et al., 2006; Baristeas et al., 2012). The high frequency of pockmarks in the NW and N areas coincide with large subsurface gas anomalies 1 and 2 (Figs. 3, 7), which suggests that gas and fluids were sourced from deeper formations and were responsible for a widespread fluid expulsion event. The presence of buried pockmarks (large-giant) and mega pockmarks (1' and 2') on the URU suggest that the older, "fossil" pockmarks were buried by the Quaternary sediments, and that renewed fluid escape activity produced the present-day seabed pockmarks, which in turn implies at least two fluid venting events. Mega-pockmarks 1'and 2' formed when the URU was not covered by sediments and fluid leakage continued later on in the same location, resulting in the formation of mega-pockmarks 1 and 2 on the seabed. We suggest that the loading by the marine ice sheet during LGM might have led to an increase in pressure and a decrease in temperature, forming favourable conditions for gas hydrates to form, which in turn acted as a seal for vertically migrating fluids, whilst the base of the GHSZ was shifted down (Fig. 11a). Deglaciation following the LGM, accompanied by the sediment erosion due to ice streaming probably led to an upward shift of the GHSZ due to increased seabed temperature and reduction in pressure as the ice sheet decoupled, which in turn led to hydrate destabilisation. Overpressure due to an increased volume of free gas below the GHSZ resulted in the migration of free gas through seismic pipes, leading to the formation of pockmarks.The pockmark distribution (Fig. 7) and their relative sizes (Fig. 5f) suggest that a large area was affected by fluid and gas leakage through acoustic pipes and pockmarks, which indicates a widespread overpressure release regime. Larger area is affected by pockmarks on the URU than on the seabed, which in turn suggests that the first fluid escape event recorded on the URU was either more vigorous compared to the more recent one recorded on the seabed or more time was available for pockmark formation. Additionally, the presence of BSR (gas anomaly 1) today points towards ongoing gas supply forming hydrates, thus suggesting continuous leakage from the reservoir.

### *5.2.2. URU depressions: Glaciotectonics vs. gas escape*

The size and density of the mega-pockmarks and depressions described in this study is similar to others found in the Gulf of Mexico, the Barents Sea, the North Sea and offshore New Zealand, where the destabilisation of marine gas hydrates has been proposed as the main driving force for the development of these features (e.g. Prior et al., 1989; Solheim and Elverhøi, 1993; Long et al., 1998; Fichler et al., 2005; Davy et al., 2010). In the North Sea, buried Quaternary mega-pockmarks are much more abundant than in the Barents Sea, but likewise, they are located in the vicinity of hydrocarbon discoveries, shallow gas accumulations and regional faults (Fichler et al., 2005).

Since the URU has a glacigenic origin (Andreassen et al., 2008 and refs. therein) and elongate depressions have been reported elsewhere in the Barents Sea (Rafaelsen et al., 2002; Andreassen et al., 2008), glacial geomorphology (hill-hole pair landforms) has been drawn to our attention as another potential mechanism for the formation of the depressions. The hill-hole pair landform consists of a single positive relief feature (hill) immediately in the down flow direction from a source depression. The hill is formed from ice shoved material and is about the same size as the hole and can provide indication of ice flow (Ottesen et al., 2005). However, it is interesting that no positive relief features at the rims or down flow of the depressions were observed (Fig. 6b), which would otherwise support this mechanism. Kettle holes or melt water cratering can also result in circular landforms. Isolated ice bodies melt under or are surrounded by glacial till, forming circular depressions as the ice blocks melt (Benn and Evans, 2010). Depressions 3' and 4' do not have typical pockmark geometry and thus may be a attributed to glaciotectonic erosion. The observed lack of associated hill in a hill hole-pair could have resulted from both glaciotectonic erosion and long distance material transportation by grounded ice or ice streams. Thus we do not excluded this mechanism as buried consolidated hills have been found on the URU in the NW Barents Sea, composed of Cretaceous sedimentary rocks and embedded within glacigenic sediments, with the associated depressions located some 20 km upstream (Sættem et al., 1992; Sættem, 1994).

The prevalence of two mega pockmarks (1 and 2) on the seabed (Fig. 6a, c-e) implies their preservation, whilst the other depressions on the URU (Fig. 6b) were draped or buried by the glacigenic deposits. If the depressions were caused by glaciotectonics, with subsequent till deposition, all of the URU depressions would be expected to have been buried. It must be considered that the mega pockmarks 1' and 2' on the URU could also be due to pull down of the reflections beneath the seabed mega pockmark 1 and 2 as the water velocity inside the pockmarks is much lower compared to the bedrock sediments next to these pockmarks and existence of pull downs beneath the mega pockmark 1' (Fig 6b) might support this theory. Nonetheless, the fact that the dipping reflections underlying the URU mega pockmarks 2' are truncated against the pockmark base (Fig. 6c,e), rules out this hypothesis, although this may not be the case for mega pockmark 1' (Fig. 6c, d). Additionally, observed discontinuous reflections (Fig. 6c-i) and fault networks directly beneath the mega pockmarks (Figs. 6, 8) points to the fact that processes related to glacial tectonics alone are insufficient to explain their origin. Another mechanism for the formation of circular depressions involves gas venting commonly observed in many sedimentary basins (Judd and Hovland, 2007). Crater-like seabed features form as a result of gas induced doming due to overpressured gas accumulations in the shallow subsurface. Fracturing and collapse of sediments above the overpressure zone, releases gas, while suspending sediment in the water column (Judd and Hovland, 2007). Rapid sedimentation may bury first generation of pockmarks, however if the gas supply continues, new pockmarks may be created, given that overpressure exists and the seal is breached (Cathles et al., 2010). Formation of pockmarks can be induced by earthquakes, tsunamis and storm waves (Judd and Hovland, 2007). As the Barents Sea shelf became ice free, post glacial earthquakes could also have produced subsurface fluid movements and further escape of fluids (Arvidsson, 1996; Leynaud et al., 2009). Hence a fluid/gas venting episode provides a more convincing argument for the genesis of these mega pockmarks and may also explain their kilometer scale dimensions.

Recent numerical modelling for the Niger delta pockmarks revealed that giant pockmarks (>1 km wide) have been caused by the dissolution of gas hydrates (Sultan et al., 2010). The pockmark formation was thought to have been triggered by discontinuation of gas flow through faults into the GHSZ or by decrease of the temperature at the seabed (Sultan et al., 2010). Similar size features have been recorded offshore New Zealand, formed due to hydrate destabilisation as a result of sea-level drops and seabed temperature increase (Davy et al., 2010). This is an additional mechanism for the formation of mega-pockmarks.

The identified mega pockmarks are located in the hanging wall of the NS fault, with reactivated and Paleocene-E. Eocene faults beneath (Fig. 6 c-g), which suggests that their development could be structurally controlled (Figs. 6, 8). It is accepted that pockmarks can form parallel to the fault strike (León et al., 2010) and may be subsequently modified by fluvial or current activity (Andresen et al., 2009; Sun et al., 2011). Depressions 2', 3' and 4',present similar orientations, with the long axes trending 150-165N (Fig 6b). This could imply current-induced erosion active during or after the formation of these depressions, with the long axes representing the direction of paleo-currents. Since the strike trend of the MSGLs on the URU is 140-160N, similar to the long axis of the depressions 2', 3' and 4' (150-165N), it is likely that the original morphology modification resulted from erosion by ice streams. This may indicate that the depressions and mega-pockmarks were formed during or after the ice streams were operating as the ice sheet retreated. Another scenario may be a combination of continued fluid flow coupled together with glaciotectonic processes, forming depressions without hill-hole pairs. In turn, the closely located mega-pockmarks may coalesce and become a laterally composite depression.

Overall, an area of ~14 km$^2$ on the seabed and ~70 km$^2$ on the URU surfaces was affected by mega pockmarks and depressions in our study area. In our case, the proximity to the regional faults also provides the source of thermogenic fluids from the Albatross and Askeladd reservoirs (Fig. 3). The existence of smaller pockmarks, to the north of the mega pockmarks along the URU, indicates that a coeval gas venting event took place over a large area.

The formation of sediment waves and erosion due to seabed currents will be sufficient to disturb the GHSZ. Erosion of low permeability sediments can create a permeable connection between the seabed and the free gas underlying the GHSZ, resulting in methane release (Holbrook et al., 2002; Bangs et al., 2010). Large melt water outflow events accompanying the deglaciation and warmer Atlantic water flux following the deglaciation (Sarnthein et al., 1995; Siegert et al., 2001) possibly had the effect of further increasing the bottom water temperature (Kennett et al., 2000) and causing further hydrate destabilisation, resulting in formation of seabed pockmarks. Such a mechanism has been proposed for the formation of the Norwegian Channel pockmarks (Forsberg et al., 2007).

The size of the mega-pockmarks might also be related to the vigor of the gas escape event or the large subsurface extent of the hydrate deposits, implying that a gas escape event could have taken place locally producing clustered kilometer scale blowout features. We separate the study area into two provinces, characterised by differences in fluid flow regimes. The northern province may resemble widespread gas and fluid flow area and is characterised by present day BSR occurrence (gas anomaly 1), seismic pipes and large-giant pockmarks, suggest that a constant influx of gas is supplied to the GHSZ in order to maintain the present day BSR. However, it is difficult to say whether the fluid escape in the study area is active today, and recent B subsurface sediment sampling within the pockmarks, biomarker and microbial activity analyses from the SW Barents Sea suggest that the thermogenic fluid venting was likely to be a paleo event (Boitsov et al., 2011; Nickel et al., 2012). The southern province is characterised by mega-pockmarks, possibly related to blow out type events, without seismic pipes and lacking evidence of a BSR, which would suggest that the fluid flow in this area has stopped.

### 5.3. Triggers and timing for fluid escape

A 2D and 3D petroleum system model for the Hammerfest Basin (Cavanagh et al., 2006; Rodrigues et al., 2011) showed that the main Triassic source rocks have been mature and generating hydrocarbons since the Late Triassic (Kobbe Fm) and Early Cretaceous (Snadd Fm), whilst the Upper Jurassic source rock (Hekkingen Fm) matured during the Early-Late Cretaceous(Fig. 2). Hydrocarbon generation is thought to have stopped during Oligocene-Miocene exhumation (Fig. 2). The main reservoir filling from the Triassic source rocks were reported to take place between 65-30 Ma, whilst Jurassic sources contributed between 40-2.5 Ma (Rodrigues et al., 2011). Remigration of hydrocarbons is thought to have been active during this time due to gas expansion, reservoir structure tilt and caprock fracturing in the SW Barents Sea (Ohm et al., 2008). Fault reactivation during late Paleocene - early Eocene would have had an impact on the hydrocarbon leakage as the reservoir structures have already been filled by this time (Fig. 2). In the Barents Sea shelf, preglacial uplift could have generated significant overpressure in the Cenozoic strata due to western margin tilting (Faleide et al., 2008), thus causing lateral transfer of pressure. During the preglacial uplift, the EW and NS trending faults in the Hammerfest Basin provided vertical migration pathways for deeper thermogenically derived fluids (Ostanin et al., 2012), similar to what has been reported in other areas such as West Africa and Spitsbergen (Knies et al., 2004; Gay et al., 2006; Anka et al., 2012). Additionally during the glaciations, the effect of ice loading and unloading may have caused further leakage of water and hydrocarbons due to reservoir overpressure development (Lerche et al., 1997; Cavanagh et al., 2006), spill from structures and renewed regional fault reactivation (Fjeldskaar et al., 2000). The thermodynamic stability of gas hydrates might have also been influenced as large scale shelf erosion and litho and hydrostatic pressure fluctuated during multiple glacial cycles (Laberg et al., 2011; Cavanagh et al., 2006). The pressure decrease effect due to the ice sheet removal during the deglaciations would be enhanced as the seabed temperature also increased. At the seabed, this mechanism may have caused relatively rapid destabilisation of gas hydrates over a possible time span of <20 years (Nisbet, 2002), forming pockmarks ranging from 150 m to 11 km wide (Davy et al., 2010).

However, it can take longer for the temperature change to propagate until the base of the GHSZ. Subsequently, reservoir gas expansion in response to overburden erosion may lead to leakage of hydrocarbons and result in fluid escape events due to increased overpressure buildup. Based on the identified fluid flow indicators on the seabed and the URU, at least two major fluid escape events must have taken place. We propose that the leaked hydrocarbons were trapped and stored as structure II gas hydrates due to favourable pressure-temperature conditions during the presence of the ice sheet. Once the ambient conditions change as the ice retreats and sediment temperature increases, overpressure buildup is relieved by leakage and pockmarks are thus produced.

The timing of the fluid venting is not easy to constrain. The URU in the Barents Sea is a polycyclic surface, representing erosion over the last 2.7 million years, diverging into several unconformities on the outer shelf, namely reflectors R1 (~0.2 Ma), R5 (1.3-1.5 Ma) and R7 (2.3-2.5 Ma) (Knies et al., 2009). The presence of MSGLs on the URU surface in the Hammerfest Basin (Fig. 4) indicates operation of fast moving ice streams, which prevailed after the time of R5 on the outer shelf, indicating a change in glacial style from erosion to aggradation (Knies et al., 2009). This fact restricts the URU in our study to 1.5 Ma or younger. At least eight glacial advances reached the shelf break, since R5, delivering vast volumes of sediments to the shelf break at high rates (Knies et al., 2009; Laberg et al., 2011). However, since about 0.7 Ma glacial erosion over the Barents Sea shelf took place mainly beneath paleo ice streams (Laberg et al., 2011) with about 440-530 m of net eroded sediments being transported from the shelf to the western margin (Laberg et al., 2011). The existence of MSGLs on the URU implies that ice streams were operating at the time in the study area, whilst the ploughmarks (Fig. 4b) are likely to have been caused by ice-sheet calving, indicating proximity to the ice sheet during deglaciation. Additionally geotechnical drillings of the glacigenic successions in the SW Barents Sea reveal several tills and glaciomarine deposits above the URU (Saettem, 1991; Sættem et al., 1992) which implies that the LGM did not erode down the URU. Thus the URU in this area may represent initial stages of the deglaciation as the ice sheet was retreating and could be correlated to the onset of ice free conditions, after one of the glaciations prior to the Late Weichselian, but younger than ~0.7 Ma. Recent work using high resolution P-cable seismic data on Mid Norwegian margin showed that three episodic overpressure-induced fluid escape events took place shortly after the Weichselian, Saalian and Elsterian glaciations (Plaza-Faverola et al., 2011). We propose that similar processes operated in our study area, governed by the waxing and waning of the ice sheets.

On the other hand, the seabed reflector marks the top of the glacigenic sediments deposited since the last deglaciation following the LGM. During the late Weichselian, the ice streams reached the western shelf edge twice (Sættem et al., 1992; Laberg and Vorren, 1995), prior to 22 cal ka BP and second after 19 cal ka BP (Sættem et al., 1992; Laberg and Vorren, 1995; Rüther et al., 2011). Based on the reconstruction of ice streams (Ottesen et al., 2005; Winsborrow et al., 2010), our study area is thought to have been under the ice sheet ~19 cal ka BP and was ice-free from 17-16 cal ka BP (Rüther et al., 2011), whilst the Barents Sea shelf was completely ice free around 15 cal ka BP (Winsborrow et al., 2010). . Therefore, the oldest fluid flow event on the URU must be much older than the Late Weichselian , whilst the more recent event recorded on the present-day seabed could have been around 17-16 cal ka BP, when the study area became ice free. This implies that the glacial retreat in the study area occurred over a time span of one thousand years. Over this short time, a large flux of thermogenic gases might have been released into the hydrosphere, resulting in the observed seabed pockmarks and mega-pockmarks. In both cases, the URU and the seabed horizons hold evidence of iceberg scouring and MSGLs, which would imply that fluid venting took place after the ice retreated, during the early stages of the deglaciation.

*Conceptual model for fluid escape*

Figure 12 summarises our proposed conceptual model for the gas leakage and the underlying control of the hydrocarbon plumbing system of the study area.

During the ice loading prior to the late Weichselian (<0.7Ma) intensive ice loading, low basal temperatures dominate. Thermogenic fluids leak from the Jurassic reservoir through EW and NS trending tectonic faults networks and are sequestered as thick zone of gas hydrates (Fig. 12a). As the ice sheet retreats, base of the GHSZ shifts whilst fluid flow features formed on the URU (Fig. 12b)

Following the LGM (~19 cal ka BP, Fig. 12c), as the ice sheet retreated over the Hammerfest Basin, ice streams rapidly removed the overburden, resulting in a shorter distance between the seabed and the base of the GHSZ (Fig. 12d). As the ice decoupled from the seabed, water column pressure dominated the stability of hydrates and increased seabed temperature led to an upward shift in the GHSZ. This caused overpressure to develop as gas hydrates melted, resulting in regional fluid leakage.

Following the complete deglaciation (~17-16 cal ka BP) and deposition of glacial tills and reworked sediment, pockmarks form as a second fluid venting episode, whilst evidence of a BSR indicate continued fluid flow at present day (Fig. 12e).

## 6 Summary and conclusions

Analysis of an industry quality 3D seismic dataset in the Hammerfest Basin reveals an extensive and complex plumbing system above the Snøhvit and Albatross gas fields. Fluid and gas leakage is manifested on the present-day seabed as abundant pockmarks, classed as mega-pockmarks (> 1 km wide), large pockmarks (< 100 m wide) and giant pockmarks (100-300 m wide). Buried depressions, mega-pockmarks and buried large-giant pockmarks have also been identified on the Upper Regional Unconformity (URU), which marks the base Quaternary, indicating an older fluid venting episode (ca. ~<0.7 Ma to prior to Late Weichselian) . The mega pockmarks are found exclusively in the southwestern part of the study area, whereas higher concentrations of large-to-giant pockmarks are found in the north-western part, suggesting localized vigorous fluid venting in the south and widespread, probably diffuse, leakage to the north. The identified leakage features are connected to seismic pipes, deep regional faults as well as shallow intra - Paleocene faults. Buried and seabed large-giant pockmarks are much more abundant above a shallow gas anomaly, interpreted as a bottom simulating reflector (BSR). The depth of the BSR coincides with the estimated base of the stability zone for a thermogenically-derived gas hydrate with a ~90 mol% methane, which is the composition of the Snøhvit gas at that depth based on PVT calculations. This indicates that favourable conditions for gas hydrates formation are present in this area. Deep-regional tectonic faults act as migration avenues for ascending thermogenic fluids from the Jurassic reservoirs, which are then transported through shallow intra-Paleocene faults, connected to seismic pipes. We propose that hydrocarbon leakage from the Jurassic reservoirs provided a source of thermogenic methane for the local formation of gas hydrates in the areas where the conducting fault networks are present.

At least two fluid venting and gas leakage events took place in the study area. The oldest one, which may have taken place during a deglaciation phase (~<0.7 Ma to prior to Late Weichselian), one was either more vigorous or lasted longer, as documented by abundant buried pockmarks and six mega-pockmarks on the URU. The youngest fluid flow venting event, evidenced by the present-day seabed features, took place shortly after the Last Glacial Maximum (LGM) during the deglaciation of the study area, estimated to have been around ~17-16 cal ka BP. Hence, we propose that the destabilization of thermogenic gas hydrates during the deglaciation resulted in formation of the observed pockmarks and mega pockmarks. Consequently, a high methane flux is expected to input into the hydrosphere following the two leakage episodes. Finally, the large number of fluid flow and gas leakage structures identified in this work indicate potential hazards for future exploration, production facilities and carbon capture/sequestration projects in the greater Snøhvit area.

## 7 Acknowledgments

This research is funded by the Helmholtz Association's Initiative and Networking Fund in the framework of Z. Anka's Helmholtz-University Young Investigator Group and is part of the ongoing PhD project of I. Ostanin. Statoil ASA Harstad is thanked for providing the STO306 seismic and well data. Lundin Petroleum is thanked for providing the additional ST8320 3D seismic data from the

Barents Sea. We are extremely grateful to very detailed and constructive comments from Karin Andreassen and Mads Huuse, which helped to improve the final version of the manuscript. We also thank the associate editor Alejandro Escalona for handling the review of the manuscript.

## 8 References

Andreassen, K., Hogstad, K., and Berteussen, K.A., 1990, Gas hydrate in the southern Barents Sea, indicated by a shallow seismic anomaly.: First Break, v. 8, no. 6.

Andreassen, K., Laberg, J.S., and Vorren, T.O., 2008, Seafloor geomorphology of the SW Barents Sea and its glaci-dynamic implications: Geomorphology, v. 97, no. 1-2, p. 157–177.

Andreassen, K., Nilssen, E., and Ødegaard, C., 2007, Analysis of shallow gas and fluid migration within the Plio-Pleistocene sedimentary succession of the SW Barents Sea continental margin using 3D seismic data: Geo-Marine Letters, v. 27, no. 2, p. 155–171, doi: 10.1007/s00367-007-0071-5.

Andresen, K.J., Clausen, O.R., Huuse, M., and Clausen Ole Rønøand Huuse, M., 2009, A giant (5.3 × 107 m3) middle Miocene (c. 15 Ma) sediment mound (M1) above the Siri Canyon, Norwegian-Danish Basin: Origin and significance: Marine and Petroleum Geology, v. 26, no. 8, p. 1640–1655.

Andresen, K.J., and Huuse, M., 2011, "Bulls-eye" pockmarks and polygonal faulting in the Lower Congo Basin: Relative timing and implications for fluid expulsion during shallow burial: Marine Geology, v. 279, no. 1-4, p. 111–127, doi: 10.1016/j.margeo.2010.10.016.

Anka, Z., Ondrak, R., Kowitz, A., and Schødt, N., 2012, Identification and numerical modelling of hydrocarbon leakage in the Lower Congo Basin: Implications on the genesis of km-wide seafloor mounded structures: Tectonophysics,, doi: http://dx.doi.org/10.1016/j.tecto.2012.11.020.

Archer, D., Martin, P., Buffett, B., Brovkin, V., Rahmstorf, S., and Ganopolski, A., 2004, The importance of ocean temperature to global biogeochemistry: Earth and Planetary Science Letters, v. 222, no. 2, p. 333–348, doi: 10.1016/j.epsl.2004.03.011.

Arvidsson, R., 1996, Fennoscandian Earthquakes: Whole Crustal Rupturing Related to Postglacial Rebound: Science, v. 274, no. 5288, p. 744–746, doi: 10.1126/science.274.5288.744.

Bahorich, M., and Farmer, S., 1995, 3-D seismic discontinuity for faults and stratigraphic features; the coherence cube: The Leading Edge, v. 14, no. 10, p. 1053–1058.

Bangs, N.L., Hornbach, M.J., Moore, G.F., and Park, J.-O., 2010, Massive methane release triggered by seafloor erosion offshore southwestern Japan: Geology, v. 38, no. 11, p. 1019–1022, doi: 10.1130/g31491.1.

Baraza, J., and Ercilla, G., 1996, Gas-charged sediments and large pockmark-like features on the Gulf of Cadiz slope (SW Spain): Marine and Petroleum Geology, v. 13, no. 2, p. 253–261, doi: 10.1016/0264-8172(95)00058-5.

Baristeas, N., Anka, Z., Di Primio, R., Rodriguez, J., Marchal, D., and Dominguez, F., 2012, Distribution of Hydrocarbon Leakage Indicators in the Malvinas Basin, offshore Argentine Continental Margin: Marine Geology, v. 332-334, p. 56–74, doi: http://dx.doi.org/10.1016/j.margeo.2012.09.011.

Van Bemmel, P., and Pepper, R., 2000, Seismic Signal Processing Method and Apparatus for Generating a Cube of Variance Values, United States Patent 6151555:.

Benn, D.I., and Evans, D.J.A., 2010, Glaciers & Glaciation: Second Edition, Hodder Education, 805 pp.

Berndt, C., 2005, Focused fluid flow in passive continental margins: Philosophical Transactions of the Royal Society A: Mathematical, Physical and Engineering Sciences, v. 363, no. 1837, p. 2855–2871, doi: 10.1098/rsta.2005.1666.

Bjørlykke, K., Hoeg, K., Faleide, J.I., and Jahren, J., 2005, When do faults in sedimentary basins leak? Stress and deformation in sedimentary basins; examples from the North Sea and Haltenbanken, offshore Norway: American Association of Petroleum Geologists Bulletin, v. 89, no. 8, p. 1019–1031, doi: 10.1306/04010504118.

Boitsov, S., Petrova, V., Jensen, H.K.B., Kursheva, A., Litvinenko, I., Chen, Y., and Klungsøyr, J., 2011, Petroleum-related hydrocarbons in deep and subsurface sediments from South-Western Barents Sea: Marine Environmental Research, v. 71, no. 5, p. 357–368, doi: 10.1016/j.marenvres.2011.04.003.

Brandes, C., Polom, U., and Winsemann, J., 2010, Reactivation of basement faults: interplay of ice-sheet advance, glacial lake formation and sediment loading: Basin Research,, p. no–no, doi: 10.1111/j.1365-2117.2010.00468.x.

Brown, A.R., 2004, Interpretation of Three-Dimensional Seismic Data: American Association of Petroleum Geologists Memoir 42, 6th Edition, Society of Exploration Geophysicists, Investigations in Geophysics no. 9, Tulsa. 541 pp.

Bulat, J., 2005, Some considerations on the interpretation of seabed images based on commercial 3D seismic in the Faroe-Shetland Channel: Basin Research, v. 17, no. 1, p. 21–42.

Bünz, S., Mienert, J., and Berndt, C., 2003, Geological controls on the Storegga gas-hydrate system of the mid-Norwegian continental margin: Earth and Planetary Science Letters, v. 209, no. 3-4, p. 291–307, doi: 10.1016/s0012-821x(03)00097-9.

Cartwright, J., Huuse, M., and Aplin, A., 2007, Seal bypass systems: AAPG Bulletin, v. 91, no. 8, p. 1141–1166, doi: 10.1306/04090705181.

Cathles, L.M., Su, Z., and Chen, D., 2010, The physics of gas chimney and pockmark formation, with implications for assessment of seafloor hazards and gas sequestration: Marine and Petroleum Geology, v. 27, no. 1, p. 82–91.

Cavanagh, A.J., Di Primio, R., Scheck-Wenderoth, M., and Horsfield, B., 2006, Severity and timing of Cenozoic exhumation in the southwestern Barents Sea: Journal of the Geological Society, v. 163, no. 5, p. 761–774, doi: 10.1144/0016-76492005-146.

Chand, S., Thorsnes, T., Rise, L., Brunstad, H., Stoddart, D., Bøe, R., Lågstad, P., and Svolsbru, T., 2012, Multiple episodes of fluid flow in the SW Barents Sea (Loppa High) evidenced by gas flares, pockmarks and gas hydrate accumulation: Earth and Planetary Science Letters, v. 331–332, no. 0, p. 305–314, doi: 10.1016/j.epsl.2012.03.021.

Clark, C.D., 1993, Mega-scale glacial lineations and cross-cutting ice-flow landforms: Earth Surface Processes and Landforms, v. 18, no. 1, p. 1–29, doi: 10.1002/esp.3290180102.

Clark, P.U., Dyke, A.S., Shakun, J.D., Carlson, A.E., Clark, J., Wohlfarth, B., Mitrovica, J.X., Hostetler, S.W., and McCabe, A.M., 2009, The Last Glacial Maximum: Science, v. 325, no. 5941, p. 710–714, doi: 10.1126/science.1172873.

Clayton, C.J., and Hay, S.J., 1994, Gas migration mechanisms from accumulation to surface: Bulletin of the Geological Society of Denmark, v. 41, no. 1, p. 12–23.

Corcoran, D. V, and Dore, A.G., 2002, Depressurization of hydrocarbon-bearing reservoirs in exhumed basin settings: evidence from Atlantic margin and borderland basins: Geological Society, London, Special Publications, v. 196, no. 1, p. 457–483, doi: 10.1144/gsl.sp.2002.196.01.25.

Davy, B., Pecher, I., Wood, R., Carter, L., and Gohl, K., 2010, Gas escape features off New Zealand: Evidence of massive release of methane from hydrates: Geophys. Res. Lett., v. 37, no. 21, p. L21309, doi: 10.1029/2010gl045184.

Dore, A.G., Corcoran, D. V, and Scotchman, I.C., 2002, Prediction of the hydrocarbon system in exhumed basins, and application to the NW European margin: Geological Society, London, Special Publications, v. 196, no. 1, p. 401–429, doi: 10.1144/gsl.sp.2002.196.01.21.

Doré, A.G., and Jensen, L.N., 1996, The impact of late Cenozoic uplift and erosion on hydrocarbon exploration: offshore Norway and some other uplifted basins: Global and Planetary Change, v. 12, no. 1-4, p. 415–436, doi: 10.1016/0921-8181(95)00031-3.

Engelhardt, H., and Kamb, B., 1993, Vertical temperature profile of Ice Stream B,: Antarctic J. US, v. 28, p. 63–66.

Faleide, J.I., Tsikalas, F., Breivik, A.J., Mjelde, R., Ritzmann, O., Engen, O., Wilson, J., and Eldholm, O., 2008, Structure and evolution of the continental margin off Norway and Barents Sea: Episodes, v. 31, no. 1, p. 82–91.

Fichler, C., Henriksen, S., Rueslaatten, H., and Hovland, M., 2005, North Sea Quaternary morphology from seismic and magnetic data: indications for gas hydrates during glaciation?: Petroleum Geoscience, v. 11, p. 331–337.

Fjeldskaar, W., Lindholm, C., Dehls, J.F., and Fjeldskaar, I., 2000, Postglacial uplift, neotectonics and seismicity in Fennoscandia: Quaternary Science Reviews, v. 19, no. 14-15, p. 1413–1422, doi: Doi: 10.1016/s0277-3791(00)00070-6.

Fleming, K., Johnston, P., Zwartz, D., Yokoyama, Y., Lambeck, K., and Chappell, J., 1998, Refining the eustatic sea-level curve since the Last Glacial Maximum using far- and intermediate-field sites: Earth and Planetary Science Letters, v. 163, no. 1-4, p. 327–342, doi: 10.1016/s0012-821x(98)00198-8.

Flemings, P.B., Liu, X., and Winters, W.J., 2003, Critical pressure and multiphase flow in Blake Ridge gas hydrates: Geology, v. 31, no. 12, p. 1057–1060, doi: 10.1130/g19863.1.

Forsberg, C.F., Planke, S., Tjelta, T.I., Svano, G., Strout, J.M., and Svensen, H., 2007, Formation of pockmarks in the Norwegian channel: Proceedings of the 6th International Offshore Site Investigation and Geotechnics Conference: Confronting New Challenges and Sharing Knowledge, 11–13 September 2007, London, UK. The Society for Underwater Technology,.

Gay, A., Lopez, M., Cochonat, P., Séranne, M., Levaché, D., and Sermondadaz, G., 2006, Isolated seafloor pockmarks linked to BSRs, fluid chimneys, polygonal faults and stacked Oligocene-Miocene turbiditic palaeochannels in the Lower Congo Basin: Marine Geology, v. 226, no. 1-2, p. 25–40.

Gorman, A.R., Holbrook, W.S., Hornbach, M.J., Hackwith, K.L., Lizarralde, D., and Pecher, I., 2002, Migration of methane gas through the hydrate stability zone in a low-flux hydrate province: Geology, v. 30, no. 4, p. 327–330, doi: 10.1130/0091-7613(2002)030<0327:momgtt>2.0.co;2.

Green, P.F., and Duddy, I.R., 2010, Synchronous exhumation events around the Arctic including examples from Barents Sea and Alaska North Slope: in: Vining, B.A. & Pickering, S. C. (Eds.) Petroleum Geology: From Mature Basins to New Frontiers - Proceedings of the 7th Petroleum Geology Conference. Petroleum Geology Conference series, Geological Society, London, v. 7, p. 633–644, doi: 10.1144/0070633.

Grollimund, B., and Zoback, M.D., 2003, Impact of glacially induced stress changes on fault-seal integrity offshore Norway: AAPG Bulletin, v. 87, no. 3, p. 493–506, doi: 10.1306/08010401134.

Haney, M.M., Snieder, R., Sheiman, J., and Losh, S., 2005, Geophysics: A moving fluid pulse in a fault zone: Nature, v. 437, no. 7055, p. 46, doi: http://www.nature.com/nature/journal/v437/n7055/suppinfo/437046a_S1.html.

Heggland, R., 1998, Gas seepage as an indicator of deeper prospective reservoirs. A study based on exploration 3D seismic data: Marine and Petroleum Geology, v. 15, no. 1, p. 1–9, doi: 10.1016/s0264-8172(97)00060-3.

Holbrook, W.S., Lizarralde, D., Pecher, I.A., Gorman, A.R., Hackwith, K.L., Hornbach, M., and Saffer, D., 2002, Escape of methane gas through sediment waves in a large methane hydrate province: Geology, v. 30, no. 5, p. 467–470, doi: 10.1130/0091-7613(2002)030<0467:eomgts>2.0.co;2.

Hornbach, M.J., Saffer, D.M., and Steven Holbrook, W., 2004, Critically pressured free-gas reservoirs below gas-hydrate provinces: Nature, v. 427, no. 6970, p. 142–144.

Hovland, M., Heggland, R., De Vries, M.H., and Tjelta, T.I., 2010, Unit-pockmarks and their potential significance for predicting fluid flow: Marine and Petroleum Geology, v. 27, no. 6, p. 1190–1199.

Huuse, M., Jackson, C.A.L., Van Rensbergen, P., Davies, R.J., Flemings, P.B., and Dixon, R.J., 2010, Subsurface sediment remobilization and fluid flow in sedimentary basins: preface: Basin Research, v. 22, no. 4, p. 342–360, doi: 10.1111/j.1365-2117.2010.00488.x.

Hyndman, R.D., and Davis, E.E., 1992, A Mechanism for the Formation of Methane Hydrate and Seafloor Bottom-Simulating Reflectors by Vertical Fluid Expulsion: J. Geophys. Res., v. 97, no. B5, p. 7025–7041, doi: 10.1029/91jb03061.

Jakobsson, M., Macnab, R., Mayer, L., Anderson, R., Edwards, M., Hatzky, J., Schenke, H.W., and Johnson, P., 2008, An improved bathymetric portrayal of the Arctic Ocean: Implications for ocean modeling and geological, geophysical and oceanographic analyses: Geophys. Res. Lett., v. 35, no. 7, p. L07602, doi: 10.1029/2008gl033520.

Judd, A.G., and Hovland, M., 2007, Seabed Fluid Flow: The Impact on Geology, Biology and the Marine Environment: Cambridge University press, 475 pp.

Kennett, J.P., Cannariato, K.G., Hendy, I.L., and Behl, R.J., 2000, Carbon Isotopic Evidence for Methane Hydrate Instability During Quaternary Interstadials: Science, v. 288, no. 5463, p. 128–133, doi: 10.1126/science.288.5463.128.

Knies, J., Damm, E., Gutt, J., Mann, U., and Pinturier, L., 2004, Near-surface hydrocarbon anomalies in shelf sediments off Spitsbergen: Evidences for past seepages: Geochem. Geophys. Geosyst., v. 5, no. 6, p. Q06003, doi: 10.1029/2003gc000687.

Knies, J., Matthiessen, J., Vogt, C., Laberg, J.S., Hjelstuen, B.O., Smelror, M., Larsen, E., Andreassen, K., Eidvin, T., and Vorren, T.O., 2009, The Plio-Pleistocene glaciation of the Barents Sea-Svalbard region: a new model based on revised chronostratigraphy: Quaternary Science Reviews, v. 28, no. 9-10, p. 812–829.

Kvenvolden, K.A., 1995, A review of the geochemistry of methane in natural gas hydrate: Organic Geochemistry, v. 23, no. 11-12, p. 997–1008, doi: 10.1016/0146-6380(96)00002-2.

Laberg, J.S., and Andreassen, K., 1996, Gas hydrate and free gas indications within the Cenozoic succession of the Bjørnøya Basin, western Barents Sea: Marine and Petroleum Geology, v. 13, no. 8, p. 921–940, doi: 10.1016/s0264-8172(96)00038-4.

Laberg, J.S., Andreassen, K., Knies, J., Vorren, T.O., and Winsborrow, M., 2010, Late Pliocene-Pleistocene development of the Barents Sea Ice Sheet: Geology, v. 38, no. 2, p. 107–110, doi: 10.1130/g30193.1.

Laberg, J.S., Andreassen, K., and Knutsen, S.M., 1998, Inferred gas hydrate on the Barents Sea shelf — a model for its formation and a volume estimate: Geo-Marine Letters, v. 18, no. 1, p. 26–33.

Laberg, J.S., Andreassen, K., and Vorren, T.O., 2011, Late Cenozoic erosion of the high-latitude southwestern Barents Sea shelf revisited: Geological Society of America Bulletin,, doi: 10.1130/b30340.1.

Laberg, J.S., and Vorren, T.O., 1995, Late Weichselian submarine debris flow deposits on the Bear Island Trough Mouth Fan: Marine Geology, v. 127, no. 1–4, p. 45–72, doi: http://dx.doi.org/10.1016/0025-3227(95)00055-4.

Lerche, I., Yu, Z., Tørudbakken, B., and Thomsen, R.O., 1997, Ice loading effects in sedimentary basins with reference to the Barents sea: Marine and Petroleum Geology, v. 14, no. 3, p. 277–338, doi: 10.1016/s0264-8172(96)00059-1.

Leynaud, D., Mienert, J., and Vanneste, M., 2009, Submarine mass movements on glaciated and non-glaciated European continental margins: A review of triggering mechanisms and preconditions to failure: Marine and Petroleum Geology, v. 26, no. 5, p. 618–632, doi: DOI: 10.1016/j.marpetgeo.2008.02.008.

León, R., Somoza, L., Medialdea, T., Hernández-Molina, F., Vázquez, J., Díaz-del-Rio, V., and González, F., 2010, Pockmarks, collapses and blind valleys in the Gulf of Cádiz: Geo-Marine Letters, v. 30, no. 3, p. 231–247.

Linjordet, A., and Grung-Olsen, R., 1992, The Jurassic Snøhvit Gas Field, Hammerfest Basin, Offshore Northern Norway: in: Halbouty, M. T. (Ed.). Giant Gas and Oil Fields of the Decade 1978–1988. AAPG Memoir, v. 54, p. 349–370.

Long, D., Lammers, S., and Linke, P., 1998, Possible hydrate mounds within large sea-floor craters in the Barents Sea: Geological Society, London, Special Publications, v. 137, no. 1, p. 223–237, doi: 10.1144/gsl.sp.1998.137.01.18.

Løseth, H., Gading, M., and Wensaas, L., 2009, Hydrocarbon leakage interpreted on seismic data: Marine and Petroleum Geology, v. 26, no. 7, p. 1304–1319.

Løseth, H., Wensaas, L., Arntsen, B., Hanken, N.-M., Basire, C., and Graue, K., 2010, 1000 m Long Gas Blow-Out Pipes: Marine and Petroleum Geology, v. In Press,.

Løvø, V., Elverhøi, A., Antonsen, P., Solheim, A., Butenko, G., and Gregersen, O., 1990, Submarine permafrost and gas hydrates in the northern Barents Sea.: Norsk Polarinstitutt Rapportserie, v. 56, p. 171.

Moss, J.L., and Cartwright, J. 3D seismic expression of km-scale fluid escape pipes from offshore Namibia: Basin Research, v. 22, no. 4, p. 481–501, doi: 10.1111/j.1365-2117.2010.00461.x.

Nickel, J.C., Di Primio, R., Mangelsdorf, K., Stoddart, D., and Kallmeyer, J., 2012, Characterization of microbial activity in pockmark fields of the SW-Barents Sea: Marine Geology, v. 332-334, p. 152–162, doi: 10.1016/j.margeo.2012.02.002.

Nisbet, E.G., 2002, Have sudden large releases of methane from geological reservoirs occurred since the Last Glacial Maximum, and could such releases occur again?: Philosophical Transactions of the Royal Society of London. Series A: Mathematical, Physical and Engineering Sciences, v. 360, no. 1793, p. 581–607, doi: 10.1098/rsta.2001.0958.

NODC, 2011, National Oceanographic Data Center: World Ocean Database: http://www.nodc.noaa.gov/General/temperature.html,.

NPD, 2011, Norwegian Petroleum Directorate Factpages: http://factpages.npd.no/factpages/Default.aspx?culture=en (Acessed June 2011) :.

Nyland, B., Jensen, L.N., Skagen, J., Skarpnes, O., and Vorren, T.O., 1992, Tertiary uplift and erosion in the Barents Sea:magnitude, timing and consequences.: in: Larsen, R. M., Brekke, H., Larsen, B. T., Talleras, E. (Eds.) Tectonic modelling an its implication to petroleum geology. Norwegian Petroleum Society Spec Publ. 1. Elsevier, Amsterdam, pp 153-162,.

Ohm, S.E., Karlsen, D.A., and Austin, T.J.F., 2008, Geochemically driven exploration models in uplifted areas: Examples from the Norwegian Barents Sea: AAPG Bulletin, v. 92, no. 9, p. 1191–1223, doi: 10.1306/06180808028.

Ostanin, I., Anka, Z., Di Primio, R., and Bernal, A., 2012, Identification of a large Upper Cretaceous Polygonal Fault network in the Hammerfest Basin: Implications on the reactivation of regional faults and gas leakage dynamics, SW Barents Sea: Marine Geology, v. 332–334, p. 109–125, doi: http://dx.doi.org/10.1016/j.margeo.2012.03.005.

Ottesen, D., Dowdeswell, J.A., and Rise, L., 2005, Submarine landforms and the reconstruction of fast-flowing ice streams within a large Quaternary ice sheet: The 2500-km-long Norwegian-Svalbard margin (57°-80°N): Geological Society of America Bulletin, v. 117, no. 7-8, p. 1033–1050, doi: 10.1130/b25577.1.

O'Brien, G.W., Lawrence, G.M., Williams, A.K., Glenn, K., Barrett, A.G., Lech, M., Edwards, D.S., Cowley, R., Boreham, C.J., and Summons, R.E., 2005, Yampi Shelf, Browse Basin, North-West Shelf, Australia: a test-bed for constraining hydrocarbon migration and seepage rates using combinations of 2D and 3D seismic data and multiple, independent remote sensing technologies: Marine and Petroleum Geology, v. 22, no. 4, p. 517–549, doi: 10.1016/j.marpetgeo.2004.10.027.

Pilcher, R., and Argent, J., 2007, Mega-pockmarks and linear pockmark trains on the West African continental margin: Marine Geology, v. 244, no. 1-4, p. 15–32.

Plaza-Faverola, A., Bünz, S., and Mienert, J., 2011, Repeated fluid expulsion through sub-seabed chimneys offshore Norway in response to glacial cycles: Earth and Planetary Science Letters, v. 305, no. 3-4, p. 297–308, doi: 10.1016/j.epsl.2011.03.001.

Plaza-Faverola, A., Westbrook, G.K., Ker, S., Exley, R.J.K., Gailler, A., Minshull, T.A., and Broto, K., 2010, Evidence from three-dimensional seismic tomography for a substantial accumulation of gas hydrate in a fluid-escape chimney in the Nyegga pockmark field, offshore Norway: J. Geophys. Res., v. 115, no. B8, p. B08104, doi: 10.1029/2009jb007078.

Prior, D.B., Doyle, E.H., and Kaluza, M.J., 1989, Evidence for Sediment Eruption on Deep Sea Floor, Gulf of Mexico: Science, v. 243, no. 4890, p. 517–519, doi: 10.1126/science.243.4890.517.

Rafaelsen, B., Andreassen, K., Kuilman, L.W., Lebesbye, E., Hogstad, K., and Midtbø, M., 2002, Geomorphology of buried glacigenic horizons in the Barents Sea from three-dimensional seismic data: Geological Society, London, Special Publications, v. 203, no. 1, p. 259–276, doi: 10.1144/gsl.sp.2002.203.01.14.

Rodrigues, E., Di Primio, R., Anka, Z., Stoddart, D., and Horsfield, B., 2011, Leakage of hydrocarbons in a glacially influenced marine environment: Hammerfest Basin (Southwestern Barents Sea): Geophysical Research Abstracts,, v. 13, no. Geophysical Research Abstracts,.

Rønholt, G., Aronsen, H.A., Hellmann, T., and Johansen, S., 2008, Improved imaging of the Snøhvit field through integration of 4C OBC and dual-azimuth streamer seismic data: First Break, v. 26, no. 12, p. 61–66.

Rüther, D.C., Bjarnadóttir, L.R., Junttila, J., Husum, K., Rasmussen, T.L., Lucchi, R.G., and Andreassen, K., 2012, Pattern and timing of the northwestern Barents Sea Ice Sheet deglaciation and indications of episodic Holocene deposition: Boreas, v. 41, no. 3, p. 494–512, doi: 10.1111/j.1502-3885.2011.00244.x.

Rüther, D.C., Mattingsdal, R., Andreassen, K., Forwick, M., and Husum, K., 2011, Seismic architecture and sedimentology of a major grounding zone system deposited by the Bjørnøyrenna Ice Stream during Late Weichselian deglaciation: Quaternary Science Reviews, v. 30, no. 19–20, p. 2776–2792, doi: http://dx.doi.org/10.1016/j.quascirev.2011.06.011.

Saettem, J., 1991, Composition and properties of glacigenic sediments in the southwestern Barents Sea: Marine Geotechnology, v. 10, no. 3-4.

Sarnthein, M., Jansen, E., Weinelt, M., Arnold, M., Duplessy, J.C., Erlenkeuser, H., Flatøy, A., Johannessen, G., Johannessen, T., Jung, S., Koc, N., Labeyrie, L., Maslin, M., Pflaumann, U., et al., 1995, Variations in Atlantic Surface Ocean Paleoceanography, 50°-80°N: A Time-Slice Record of the Last 30,000 Years: Paleoceanography, v. 10, no. 6, p. 1063–1094, doi: 10.1029/95pa01453.

Siegert, M.J., Dowdeswell, J.A., Hald, M., and Svendsen, J.-I., 2001, Modelling the Eurasian Ice Sheet through a full (Weichselian) glacial cycle: Global and Planetary Change, v. 31, no. 1-4, p. 367–385, doi: 10.1016/s0921-8181(01)00130-8.

Singh, S.C., and Minshull, T.A., 1993, Velocity structure of a gas hydrate reflector.: Science, v. 260, p. 204–7.

Sloan, E.D., 1990, Clathrate Hydrates of Natural gases: Marcel Dekker. New York.

Solheim, A., and Elverhøi, A., 1985, A pockmark field in the Central Barents Sea; gas from a petrogenic source?: Polar Research, v. 3, no. 1, p. 11–19, doi: 10.1111/j.1751-8369.1985.tb00492.x.

Solheim, A., and Elverhøi, A., 1993, Gas-related sea floor craters in the Barents Sea: Geo-Marine Letters, v. 13, no. 4, p. 235–243.

Solheim, A., and Kristoffersen, Y., 1984, The physical environment Western Barents Sea, 1:500000. Sediments above the upper regional unconformity: Thickness, seismic stratigraphy and outline of the glacial history.: Norsk Polarinsitutt Skrifter, v. 179B, p. 1–26.

Sultan, N., Marsset, B., Ker, S., Marsset, T., Voisset, M., Vernant, A.M., Bayon, G., Cauquil, E., Adamy, J., Colliat, J.L., and Drapeau, D., 2010, Hydrate dissolution as a potential mechanism for pockmark formation in the Niger delta: J. Geophys. Res., v. 115, no. B8, p. B08101, doi: 10.1029/2010jb007453.

Sun, Q., Wu, S., Hovland, M., Luo, P., Lu, Y., and Qu, T., 2011, The morphologies and genesis of mega-pockmarks near the Xisha Uplift, South China Sea: Marine and Petroleum Geology, v. 28, no. 6, p. 1146–1156, doi: 10.1016/j.marpetgeo.2011.03.003.

Svendsen, J.I., Alexanderson, H., Astakhov, V.I., Demidov, I., Dowdeswell, J.A., Funder, S., Gataullin, V., Henriksen, M., Hjort, C., Houmark-Nielsen, M., Hubberten, H.W., Ingólfsson, Ó., Jakobsson, M., Kjær, K.H., et al., 2004, Late Quaternary ice sheet history of northern Eurasia: Quaternary Science Reviews, v. 23, no. 11-13, p. 1229–1271.

Sættem, J., 1994, Glaciotectonic structures along the southern Barents shelf margin, *in* (eds), W.& C. ed., Formation and Deformation of Glacial Deposits, Balkema, Rotterdam, p. 95–113.

Sættem, J., Poole, D.A.R., Ellingsen, L., and Sejrup, H.P., 1992, Glacial geology of outer Bjørnøyrenna, southwestern Barents Sea: Marine Geology, v. 103, no. 1–3, p. 15–51, doi: http://dx.doi.org/10.1016/0025-3227(92)90007-5.

Vorren, T.O., and Laberg, J.S., 1996, Late glacial air temperature, oceanographic and ice sheet interactions in the southern Barents Sea region: Geological Society, London, Special Publications, v. 111, no. 1, p. 303–321, doi: 10.1144/gsl.sp.1996.111.01.20.

Winsborrow, M.C.M., Andreassen, K., Corner, G.D., and Laberg, J.S., 2010, Deglaciation of a marine-based ice sheet: Late Weichselian palaeo-ice dynamics and retreat in the southern Barents Sea reconstructed from onshore and offshore glacial geomorphology: Quaternary Science Reviews, v. 29, no. 3-4, p. 424–442.

**List of Figures**

Figure 1. A) Regional framework of the study area showing the IBCAO bathymetry (Jakobsson et al., 2008) topography and structural elements: HB=Hammerfest Basin, FP = Finnmark Platform, LH = Loppa High, BP = Bjarmeland Platform, TB = Tromso Basin, modified from Ostanin et al., (2012). B) Ice stream and ice divide locations (Ottesen et al., 2005) and maximum ice sheet extent during the LGM (Svendsen et al., 2004). BITMF = Bear Island Trough mouth fan, STMF = Sorfjorden Trough mouth fan. Red boxes show locations of the 3D seismic data (see Fig. 3 for a detailed view).

Figure 2. Tectono-stratigraphic chart, including petroleum system elements of the Hammerfest Basin, modified from Ostanin et al., (2012) and Rodrigues et al., (2011). (See Fig. 3 for location).

Figure 3. Map of seabed pockmarks and Paleocene-Eocene shallow fluid leakage indicators interpreted using 3D and 2D seismic data. Labels A1 and A2 refer to gas anomalies 1 and 2 (see text for details).

Red outlines show location of the 3D seismic data used. The location of small pockmarks below seismic resolution was compiled from Judd and Hovland, (2007). Location of the faults and gas fields modified from Ostanin et al., (2012).

Figure 4. Evidence of glacial erosion in the study area shown on the A) The Seabed and B) the URU. (The depth depicted in two-way travel time (ms).)

Figure 5.Examples of pockmarks identified in the study area: A) Giant pockmarks (>200 m wide), B) Giant pockmarks with underlying Paleocene-E. Eocene Faults (PEEFs), C) Large pockmarks (<100 m wide), D) Pockmarks above first order reactivated faults, E) Ploughmarks above faults, F) Buried pockmarks on the URU, G). (See Table 1 for additional details on classification criteria. The insert in the right corner of each panel shown the location of the map within the STO306 3D seismic volume.

Figure 6. A) Mega pockmarks identified on the seabed and B) Buried mega pockmarks and depressions on the URU. The seismic profiles across these features are shown in inserts C-I. See text for details

Figure 7. A) Location and classification of seabed pockmarks based on size (see Fig. 5 and Table 1 for descriptions). The locations of subsurface shallow Paleocene-Early Eocene (PEEFs) and reactivated deep tectonic faults at -740 ms TWT are based on Ostanin et al., (2012). (See Fig. 2 for time slice location. B) Isopach map (in TWT) of the Quaternary sediments between the URU and the seabed. C) Map showing locations of pockmarks identified on the URU (see Fig. 5 for examples), subsurface gas anomalies and fault networks (same as in insert A).

Figure 8. A) 3D view of the seabed and B) the URU surface with structural interpretation (see Fig. 3), showing 2 seabed mega pockmarks and 6 buried mega depressions (see text for details). A complex network of faults exists above the reservoir consisting of polygonal faults, Paleocene - E. Eocene faults and regional reactivated tectonic faults, possibly responsible for transporting the thermogenic fluids from Jurassic reservoirs to shallower levels.

Figure 9. A) Seismic profile across the identified bottom simulating reflector (BSR) in gas anomaly A1 (see Fig. 3 for location). B) Interpretation of the insert A. C) Seismic attribute volume rendering of the plumbing system above BSR gas anomaly 1 (Fig. 3), showing faults cutting through the BSR and leading to seismic pipes linked to buried and present-day seafloor pockmarks.

Figure 10.A) Detailed profile across gas anomaly A2 (Fig. 3).B) Seismic attribute volume rendering of the plumbing system related to gas anomaly 2 (Fig 3), showing several seismic pipes above the edge of anomaly 2.

Figure 11. Estimated Gas hydrate stability zone (GHSZ) curves for different gas compositions and salinity (using the CSMHYD software (Sloan, 1990) , during: (a) Last Glacial Maximum (LGM), (b) interglacials and (c) present-day.

Figure 12. Conceptual proposed model for the fluid flow, thermogenic gas leakage and gas hydrate destabilisation during A) pre Late Weichselian glaciation, B) Deglaciation event forming fluid flow features on the URU, C) Last Glacial Maximum (~19 cal ka BP), D) Ice retreat in the study area ~17-16

cal ka BP and E) Ice free conditions (15 cal ka BP) and present day scenario. Calibrated ages are based on Rüther et al., (2012).

Figure 1



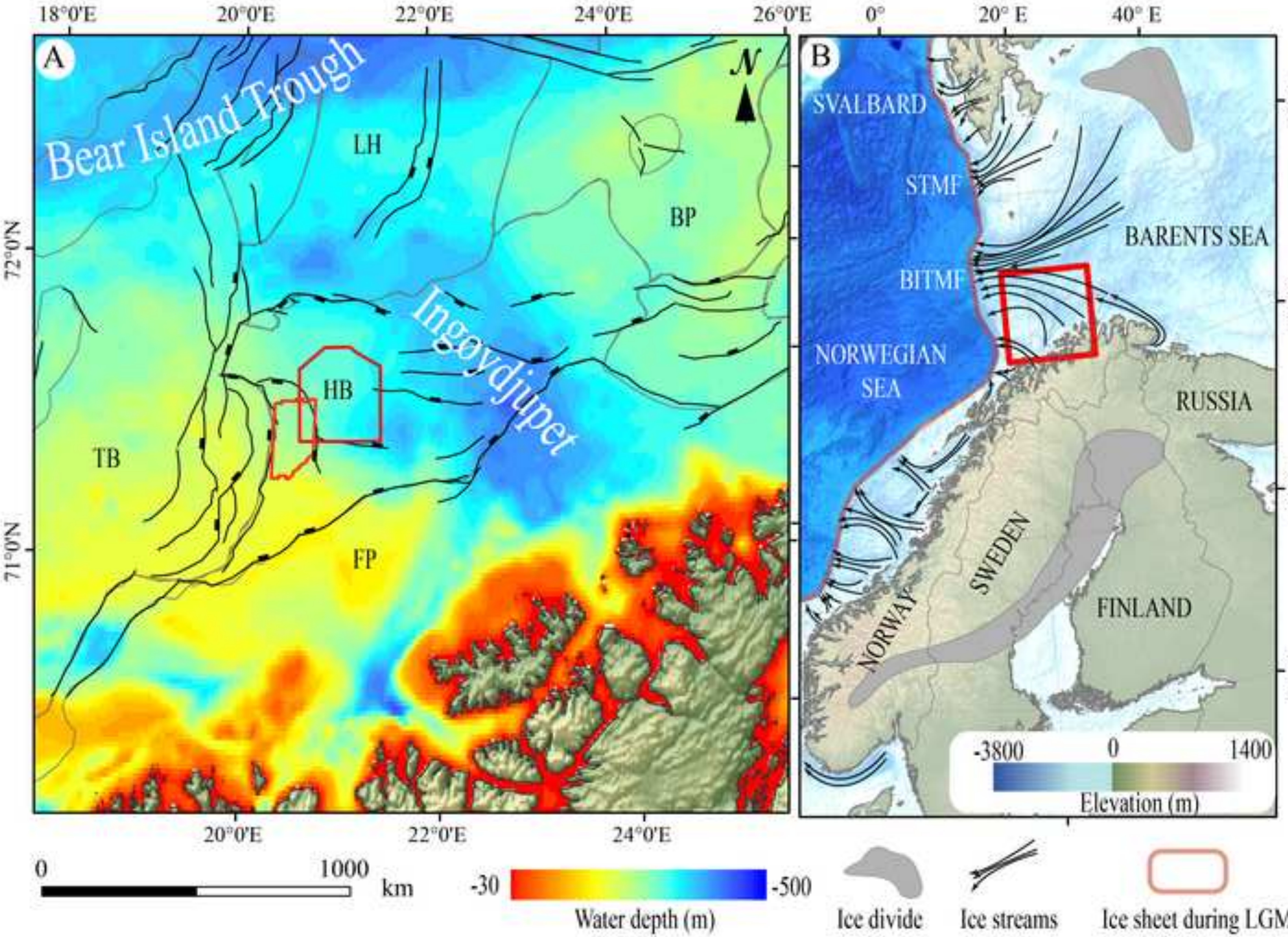
A
B
18°0'E
20°0'E
22°0'E
24°0'E
26°0'E
0°
20° E
40° E
72°0'N
71°0'N
75° N
70° N
65° N
60° N
Bear Island Trough
Ingøydjupet
LH
BP
HB
TB
FP
N
SVALBARD
STMF
BITMF
NORWEGIAN SEA
BARENTS SEA
RUSSIA
SWEDEN
FINLAND
NORWAY
-3800
0
1400
Elevation (m)
0
1000
km
-30
-500
Water depth (m)
Ice divide
Ice streams
Ice sheet during LGM

Figure 2



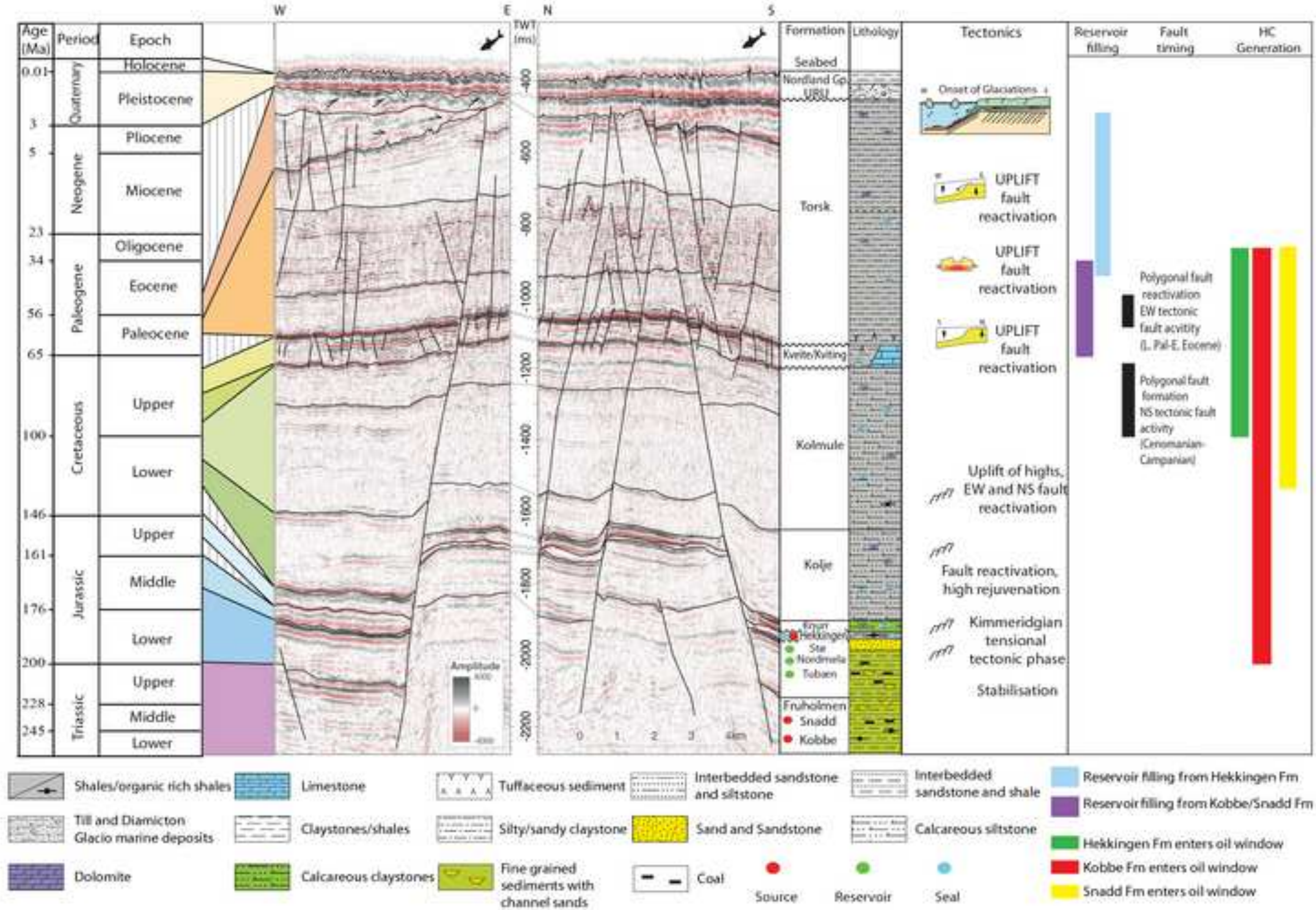

Age (Ma)
Period
Epoch
W
E
TWT (ms)
N
S
Formation
Lithology
Tectonics
Reservoir filling
Fault timing
HC Generation
0.01
3
5
23
34
56
65
100
146
161
176
200
228
245
Quaternary
Neogene
Paleogene
Cretaceous
Jurassic
Triassic
Holocene
Pleistocene
Pliocene
Miocene
Oligocene
Eocene
Paleocene
Upper
Lower
Upper
Middle
Lower
Upper
Middle
Lower
-400
-600
-800
-1000
-1200
-1400
-1600
-1800
-2000
-2200
Amplitude
0
1
2
3
4km
Seabed
Nordland Gp.
URU
Torsk
Kveite/Kviting
Kolmule
Kolje
Knurr
Hekkingen
Stø
Nordmela
Tubåen
Fruholmen
Snadd
Kobbe
Onset of Glaciations
UPLIFT fault reactivation
UPLIFT fault reactivation
UPLIFT fault reactivation
Uplift of highs, EW and NS fault reactivation
Fault reactivation, high rejuvenation
Kimmeridgian tensional tectonic phase
Stabilisation
Polygonal fault reactivation EW tectonic fault acvitity (L. Pal-E. Eocene)
Polygonal fault formation NS tectonic fault activity (Cenomanian-Campanian)
Shales/organic rich shales
Limestone
Tuffaceous sediment
Interbedded sandstone and siltstone
Interbedded sandstone and shale
Till and Diamicton Glacio marine deposits
Claystones/shales
Silty/sandy claystone
Sand and Sandstone
Calcareous siltstone
Dolomite
Calcareous claystones
Fine grained sediments with channel sands
Coal
Source
Reservoir
Seal
Reservoir filling from Hekkingen Fm
Reservoir filling from Kobbe/Snadd Fm
Hekkingen Fm enters oil window
Kobbe Fm enters oil window
Snadd Fm enters oil window

Figure 3



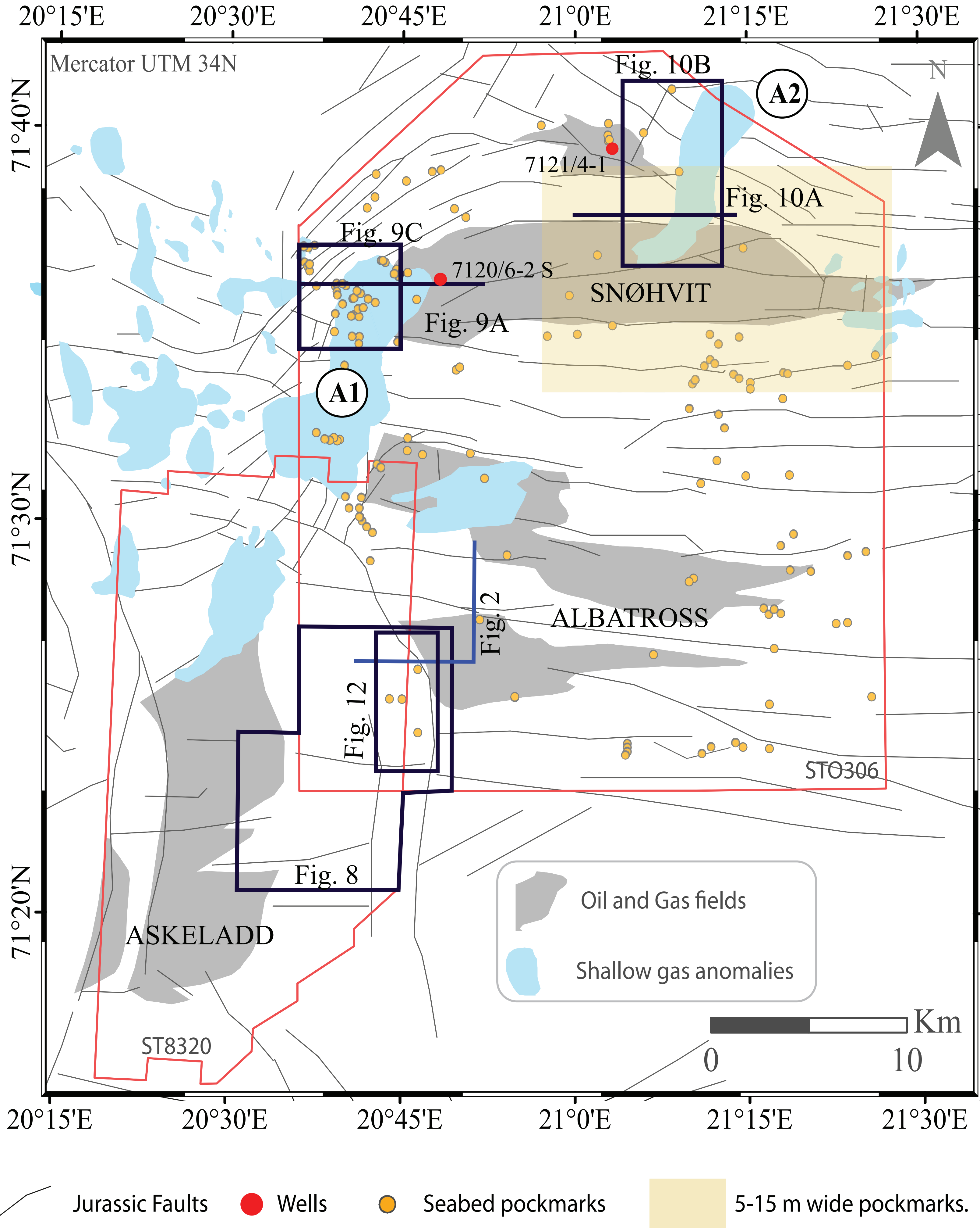

20°15'E
20°30'E
20°45'E
21°0'E
21°15'E
21°30'E
71°40'N
71°30'N
71°20'N
Mercator UTM 34N
N
Fig. 10B
A2
7121/4-1
Fig. 10A
Fig. 9C
7120/6-2 S
SNØHVIT
Fig. 9A
A1
Fig. 2
ALBATROSS
Fig. 12
STO306
Fig. 8
ASKELADD
Oil and Gas fields
Shallow gas anomalies
Km
0
10
ST8320
Jurassic Faults
Wells
Seabed pockmarks
5-15 m wide pockmarks.

**Figure 4**



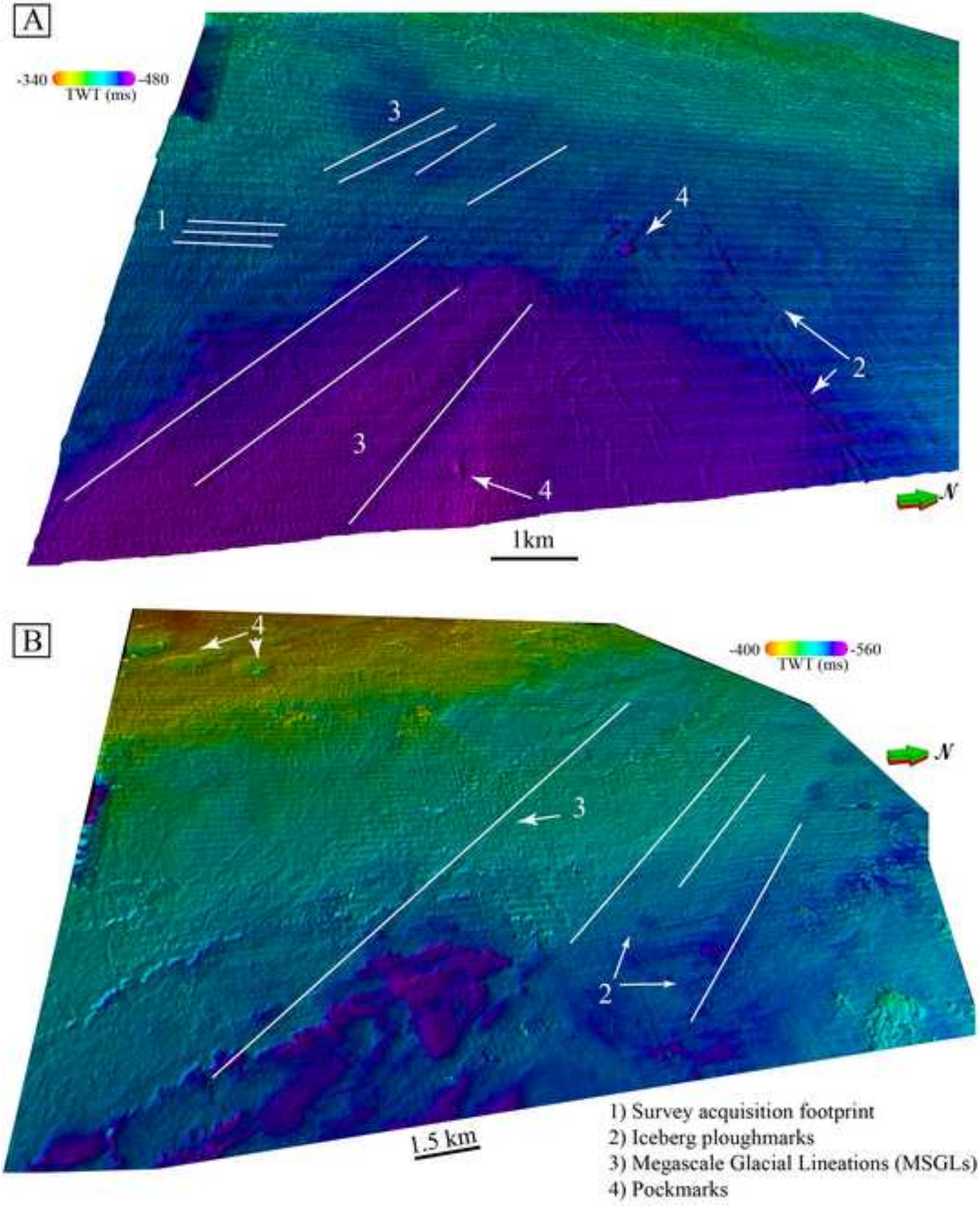


1) Survey acquisition footprint
2) Iceberg ploughmarks
3) Megascale Glacial Lineations (MSGLs)
4) Pockmarks

Figure 5



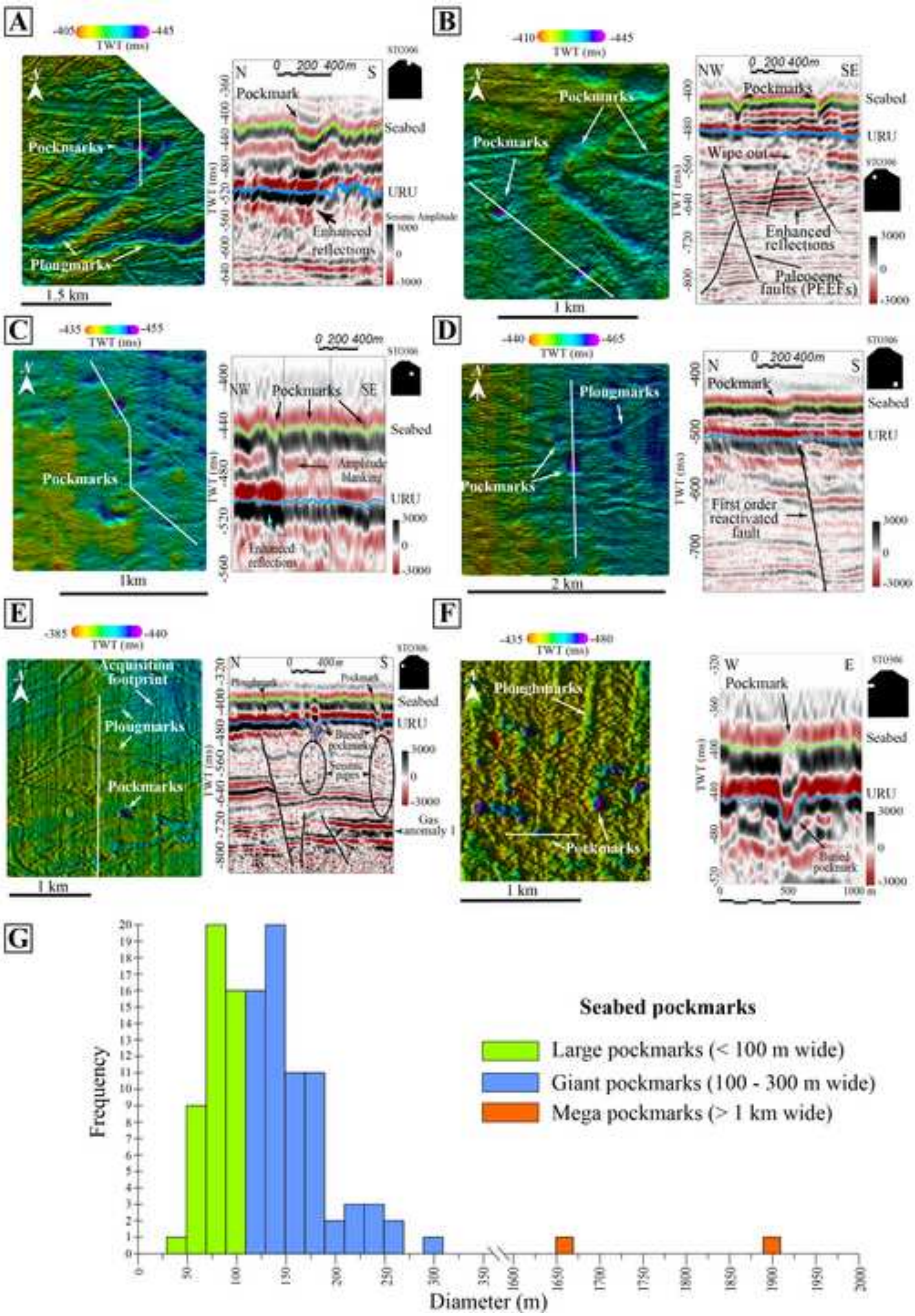
A
TWT (ms)
Pockmarks
Plougmarks
1.5 km
N
S
Pockmark
Seabed
URU
Enhanced reflections
B
TWT (ms)
Pockmarks
1 km
NW
SE
Seabed
URU
Wipe out
Enhanced reflections
Paleocene faults (PEEFs)
C
TWT (ms)
Pockmarks
1km
NW
SE
Amplitude blanking
Enhanced reflections
D
TWT (ms)
Plougmarks
Pockmarks
2 km
Pockmark
First order reactivated fault
E
TWT (ms)
Acquisition footprint
Plougmarks
Pockmarks
1 km
Buried pockmarks
Gas anomaly 1
F
TWT (ms)
Ploughmarks
Pockmarks
1 km
W
E
Pockmark
Buried pockmark
G
Frequency
Diameter (m)
Seabed pockmarks
Large pockmarks (< 100 m wide)
Giant pockmarks (100 - 300 m wide)
Mega pockmarks (> 1 km wide)

Figure 6



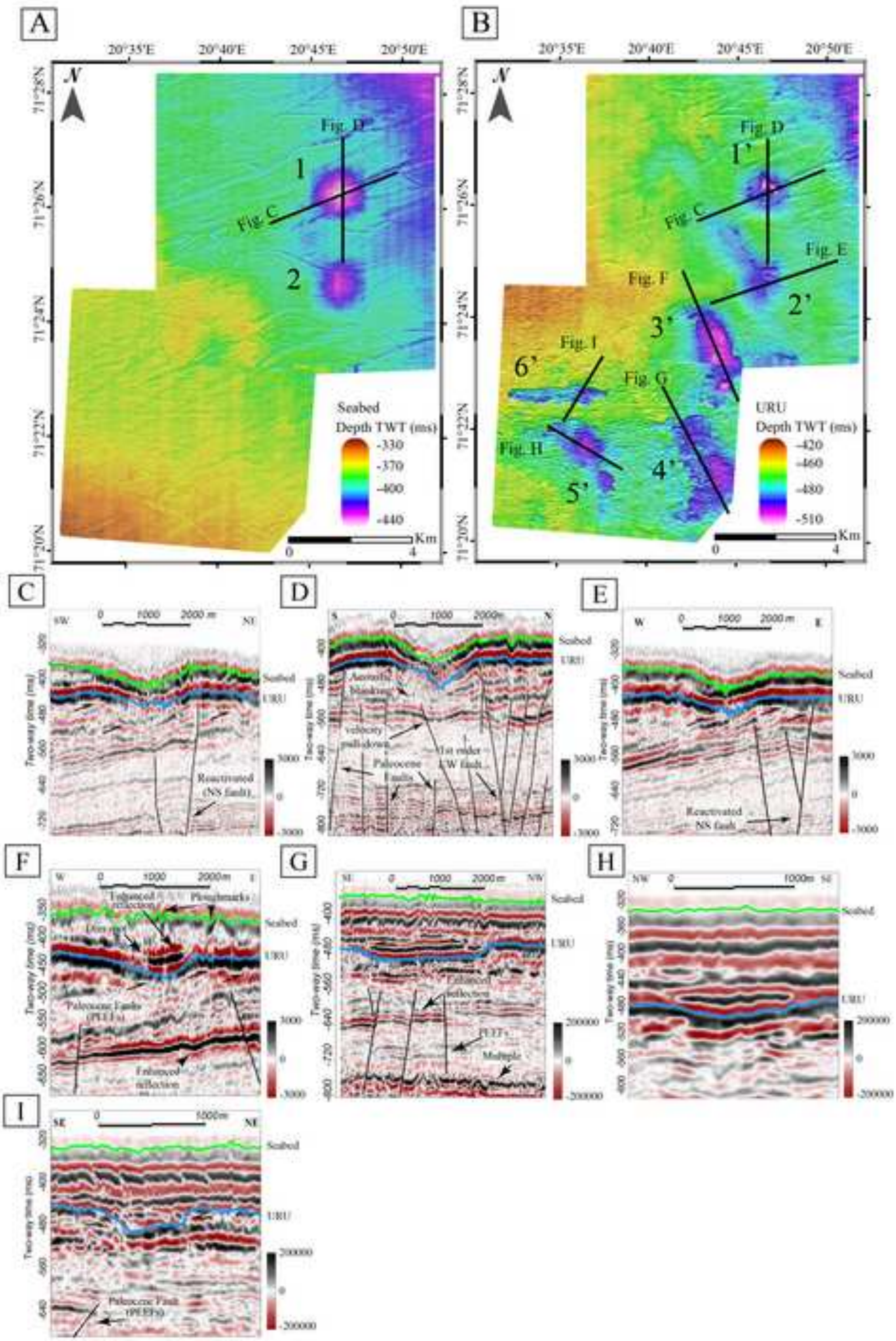
A
20°35'E
20°40'E
20°45'E
20°50'E
71°26'N
71°24'N
71°22'N
71°20'N
Fig. D
Fig. C
1
2
Seabed
Depth TWT (ms)
-330
-370
-400
-440
Km
0
4
B
Fig. E
Fig. F
Fig. G
Fig. I
Fig. H
1'
2'
3'
4'
5'
6'
URU
-420
-460
-480
-510
C
D
E
F
G
H
I
Seabed
URU
Two-way time (ms)
Reactivated (NS fault)
Acoustic blanking
velocity pulldown
1st order EW fault
Paleocene Faults
Reactivated NS fault
Enhanced reflection
Ploughmarks
Paleocene Faults (PLEFs)
PLEFs
Multiple
Paleocene Fault (PLEFs)
3000
0
-3000
200000
-200000

Figure 7



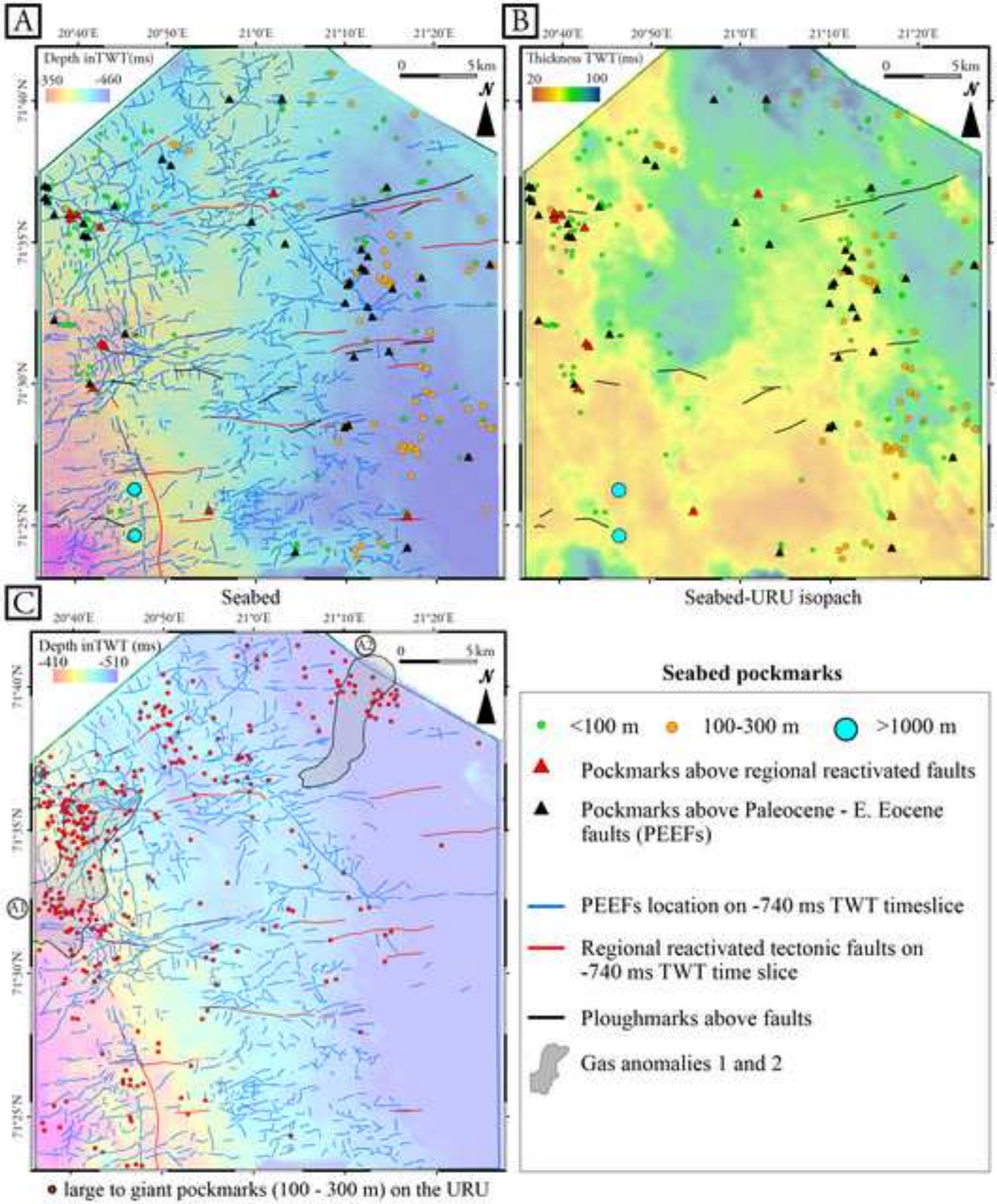
A
Depth in TWT (ms)
350
-460
0
5 km
N
Seabed
B
Thickness TWT (ms)
20
100
Seabed-URU isopach
C
Depth in TWT (ms)
-410
-510
A1
A2
large to giant pockmarks (100 - 300 m) on the URU
Seabed pockmarks
<100 m
100-300 m
>1000 m
Pockmarks above regional reactivated faults
Pockmarks above Paleocene - E. Eocene faults (PEEFs)
PEEFs location on -740 ms TWT timeslice
Regional reactivated tectonic faults on -740 ms TWT time slice
Ploughmarks above faults
Gas anomalies 1 and 2

Figure 8



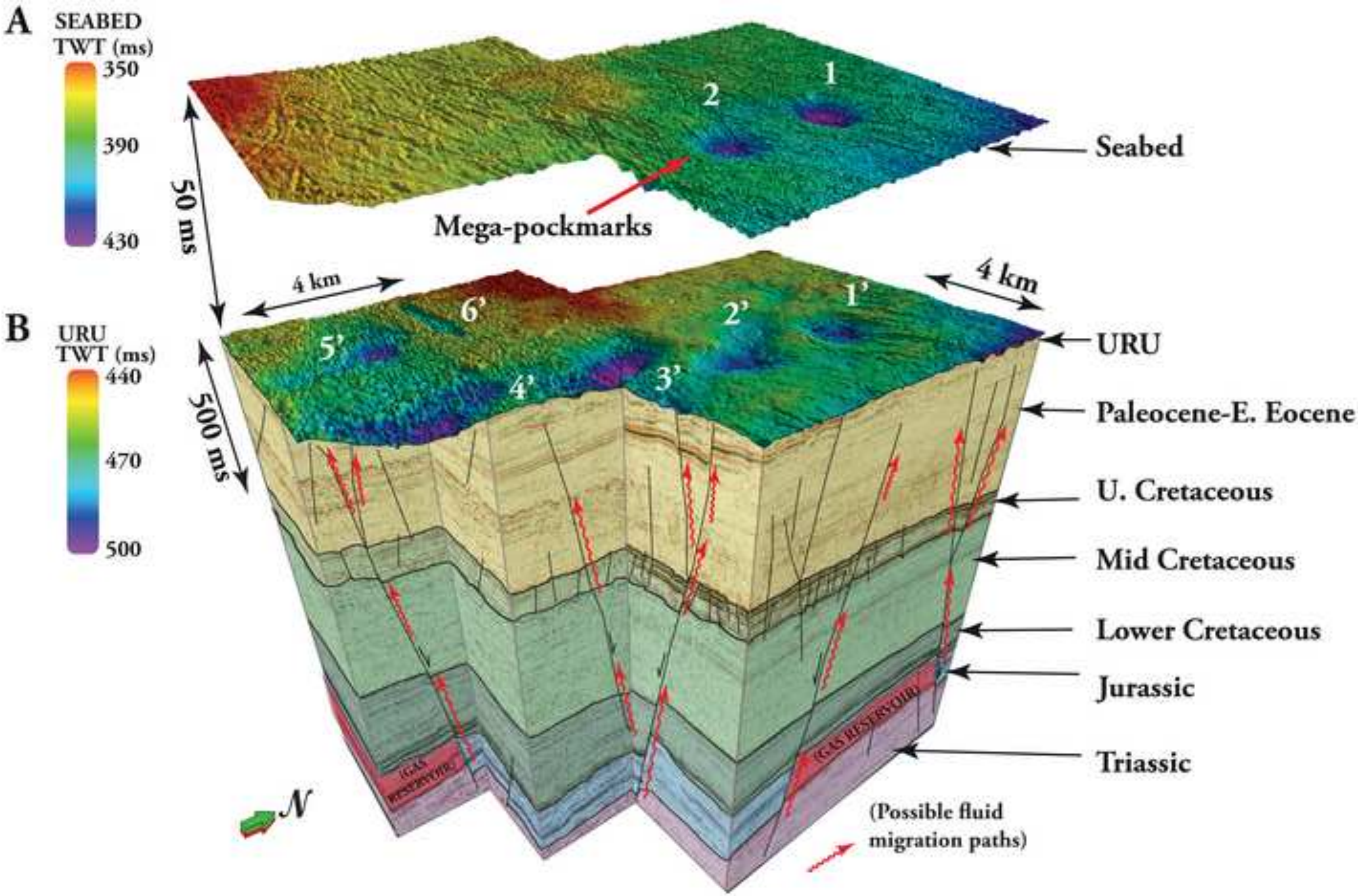
A
SEABED
TWT (ms)
350
390
430
50 ms
1
2
Seabed
Mega-pockmarks
4 km
4 km
B
URU
TWT (ms)
440
470
500
500 ms
6'
5'
4'
3'
2'
1'
URU
Paleocene-E. Eocene
U. Cretaceous
Mid Cretaceous
Lower Cretaceous
Jurassic
Triassic
GAS RESERVOIR
GAS RESERVOIR
N
(Possible fluid
migration paths)

Figure 9



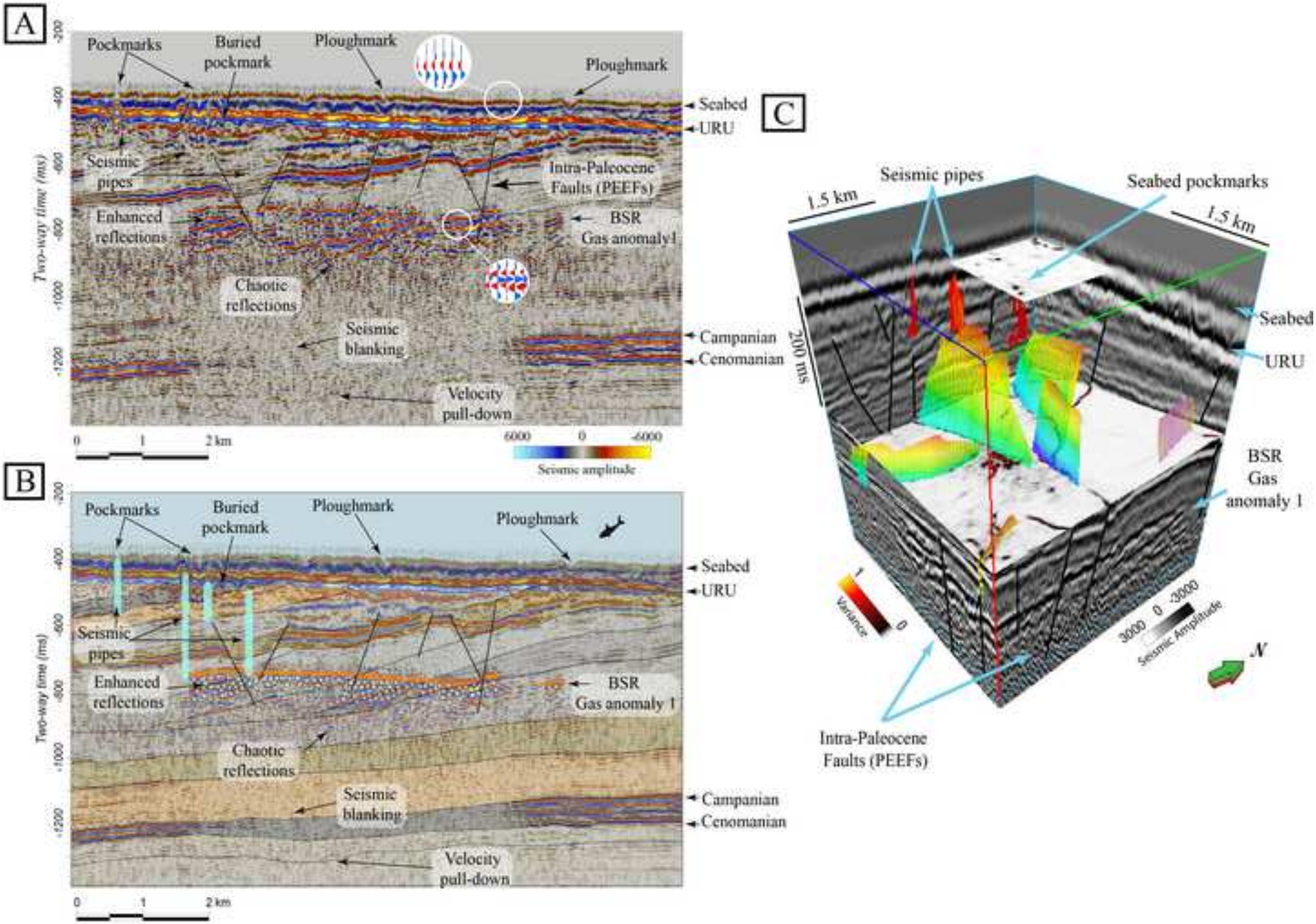

A
Pockmarks
Buried pockmark
Ploughmark
Ploughmark
Seabed
URU
Seismic pipes
Intra-Paleocene Faults (PEEFs)
Enhanced reflections
BSR Gas anomaly1
Chaotic reflections
Seismic blanking
Campanian
Cenomanian
Velocity pull-down
Two-way time (ms)
0 1 2 km
6000 0 -6000
Seismic amplitude
B
Pockmarks
Buried pockmark
Ploughmark
Ploughmark
Seabed
URU
Seismic pipes
Enhanced reflections
BSR Gas anomaly 1
Chaotic reflections
Seismic blanking
Campanian
Cenomanian
Velocity pull-down
Two-way time (ms)
0 1 2 km
C
Seismic pipes
Seabed pockmarks
1.5 km
1.5 km
200 ms
Seabed
URU
BSR Gas anomaly 1
Variance
1 0
3000 0 -3000
Seismic Amplitude
N
Intra-Paleocene Faults (PEEFs)

Figure 10



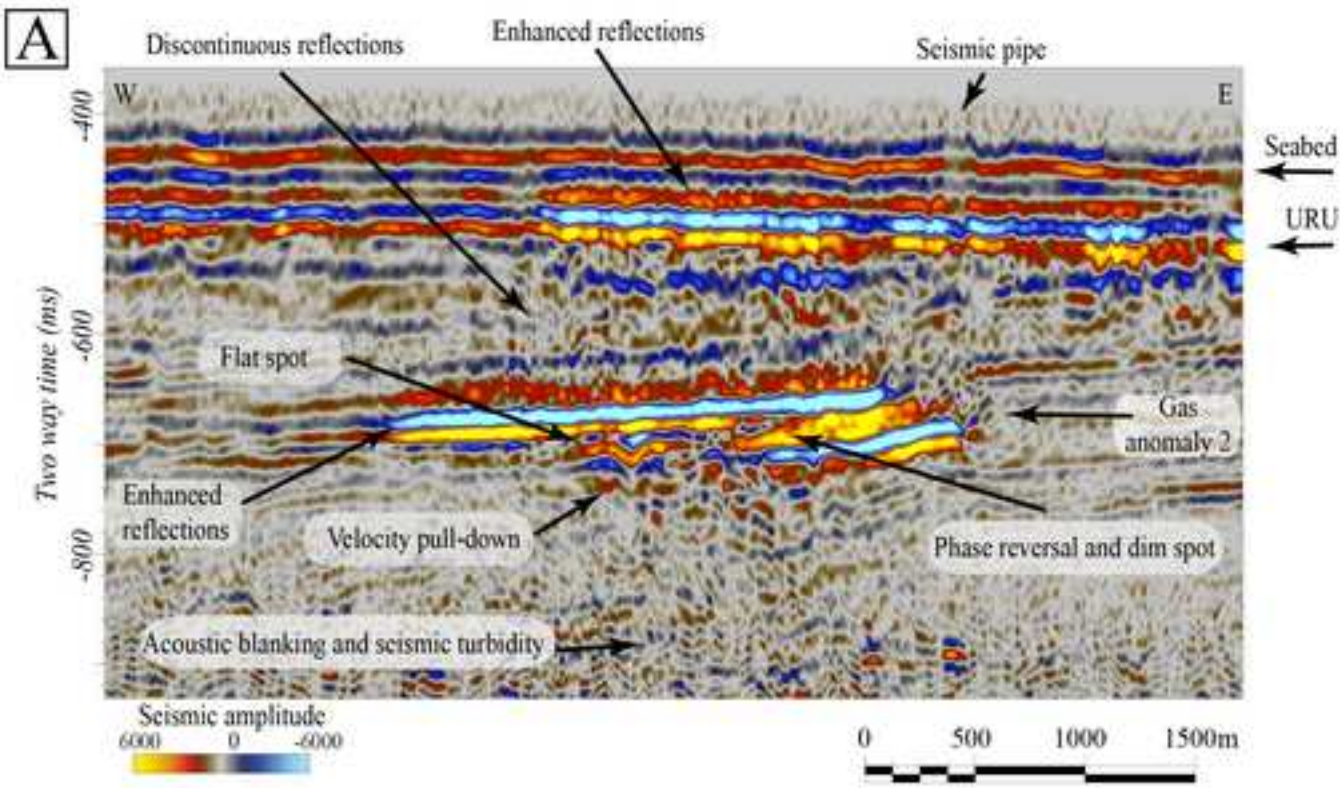
A
Discontinuous reflections
Enhanced reflections
Seismic pipe
W
E
Seabed
URU
Two way time (ms)
-400
-600
-800
Flat spot
Gas anomaly 2
Enhanced reflections
Velocity pull-down
Phase reversal and dim spot
Acoustic blanking and seismic turbidity
Seismic amplitude
6000
0
-6000
0
500
1000
1500m

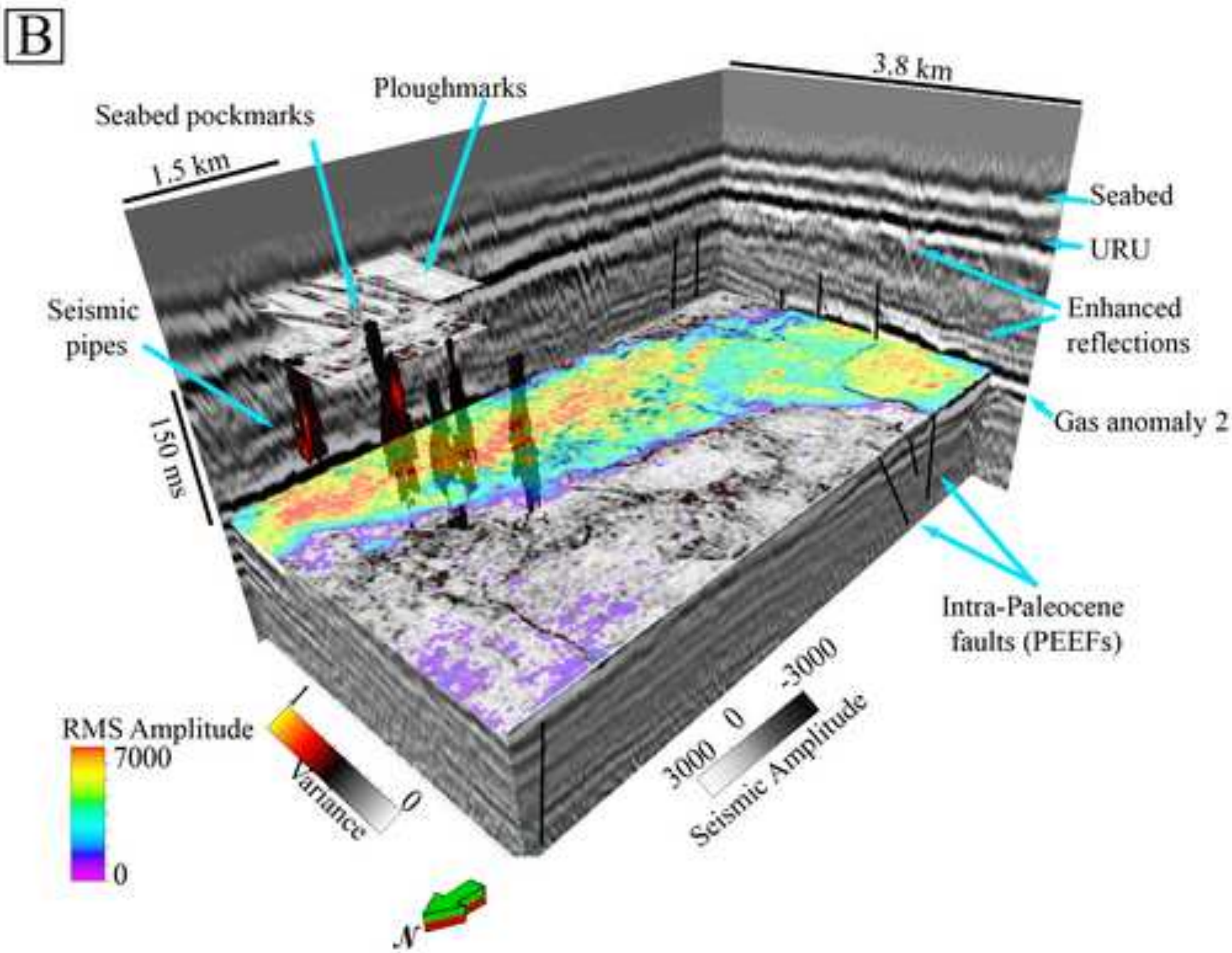
B
3.8 km
Ploughmarks
Seabed pockmarks
1.5 km
Seabed
URU
Seismic pipes
Enhanced reflections
150 ms
Gas anomaly 2
Intra-Paleocene faults (PEEFs)
RMS Amplitude
7000
0
Variance
0
3000
0
-3000
Seismic Amplitude
N

Figure 11



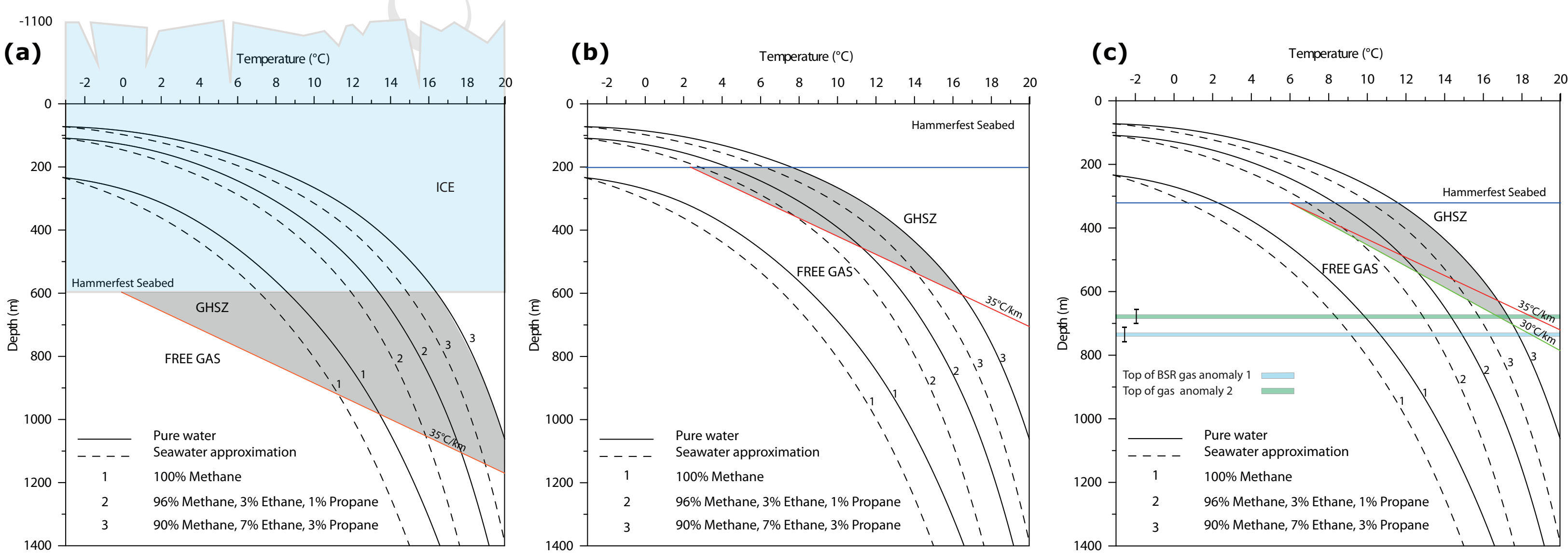
(a)
(b)
(c)
Temperature (°C)
Depth (m)
-1100
ICE
Hammerfest Seabed
GHSZ
FREE GAS
35°C/km
30°C/km
Top of BSR gas anomaly 1
Top of gas anomaly 2
Pure water
Seawater approximation
1 100% Methane
2 96% Methane, 3% Ethane, 1% Propane
3 90% Methane, 7% Ethane, 3% Propane

Figure 12



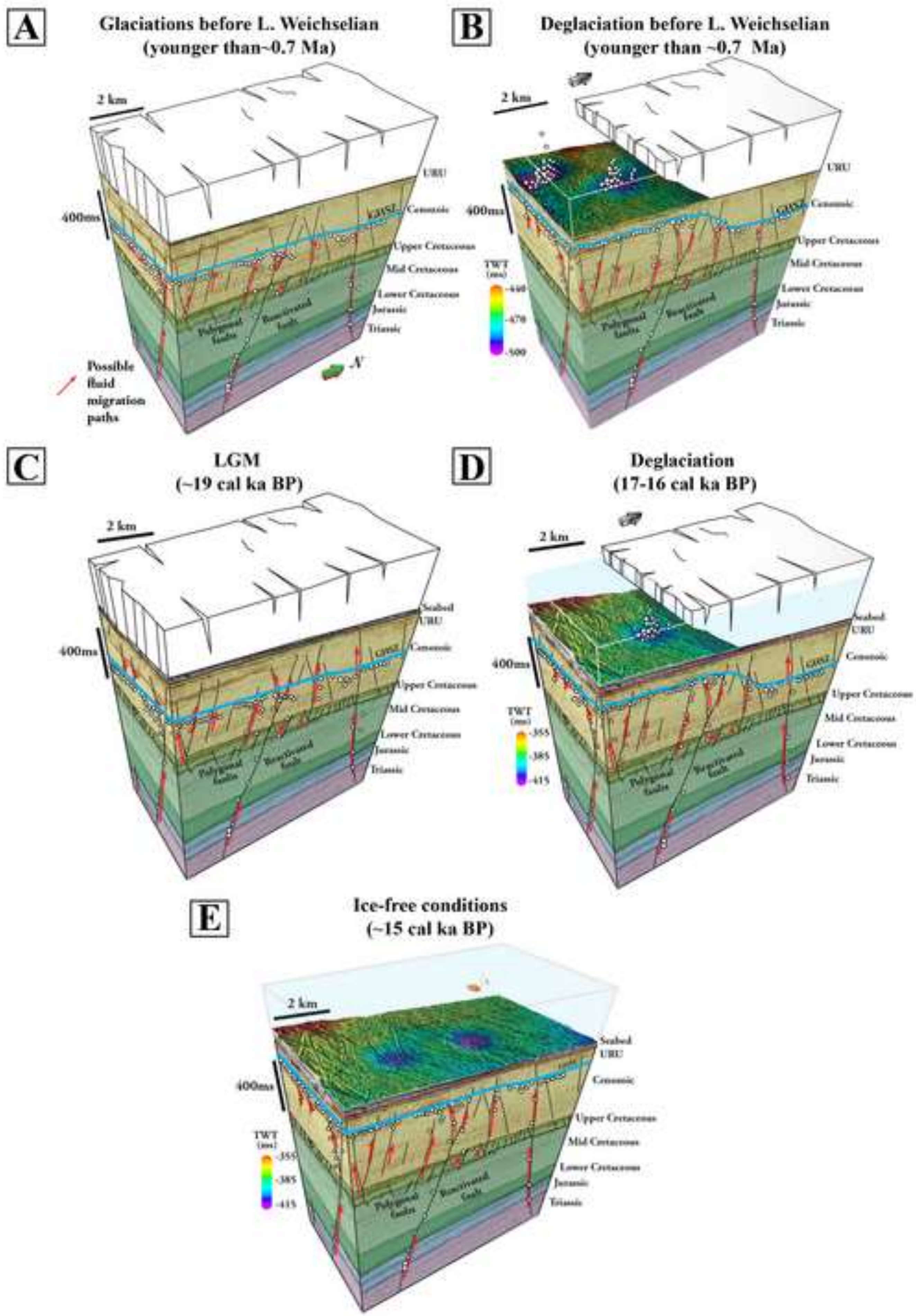
A
Glaciations before L. Weichselian
(younger than~0.7 Ma)
B
Deglaciation before L. Weichselian
(younger than ~0.7 Ma)
C
LGM
(~19 cal ka BP)
D
Deglaciation
(17-16 cal ka BP)
E
Ice-free conditions
(~15 cal ka BP)
2 km
400ms
Seabed
URU
Cenozoic
Upper Cretaceous
Mid Cretaceous
Lower Cretaceous
Jurassic
Triassic
Polygonal faults
Reactivated faults
Possible fluid migration paths
TWT (ms)
-440
-470
-500
-355
-385
-415
N

Table 1



| Feature | Dimensions | Depth | Description |
|---|---|---|---|
| Pockmarks | 5-15m (Unresolved on 3D seismic data) | < 3 m | Present on the seabed and within ploughmarks (Judd and Hovland, 2007) |
| Large pockmarks | up to 100 m | < 10 m | Encountered on the seabed and URU |
| Giant pockmarks | 100-300 m | 10-16 m | Prominent depressions on the seabed and the URU |
| Mega-pockmarks | >1 km | 20-50 m | Prominent depressions on the URU, only 2 present on the seabed |

Table 1. Description of identified pockmarks, classified based on their dimensions.